Characteristics for the Occurrence of a High-Current, Z-Pinch Aurora as Recorded in Antiquity

Anthony L. Peratt, *Fellow, IEEE*

***Abstract*—The discovery that objects from the Neolithic or Early Bronze Age carry patterns associated with high-current Z-pinches provides a possible insight into the origin and meaning of these ancient symbols produced by man. This paper directly compares the graphical and radiation data from high-current Z-pinches to these patterns. The paper focuses primarily, but not exclusively, on petroglyphs. It is found that a great many archaic petroglyphs can be classified according to plasma stability and instability data. As the same morphological types are found worldwide, the comparisons suggest the occurrence of an intense aurora, as might be produced if the solar wind had increased between one and two orders of magnitude, millennia ago.**

***Index Terms*—Aurora, high-energy-density plasma, magnetohydrodynamics (MHD) instabilities, petroglyphs, pictographs, stonehenge, Z-pinch.**

I. Introduction

ON July 9, 1962, the United States detonated a 1.4-megaton thermonuclear device in the atmosphere 400 km above Johnston Island. The event produced a plasma whose initial spherical shape striated within a few minutes as the plasma electrons and ions streamed along the Earth's magnetic field to produce an artificial aurora. Fig. 1 shows a photograph of the artificial aurora three minutes after detonation as recorded from a KC-135 aircraft.

Concomitant with the artificial aurora was a degradation of radio communications over wide areas of the Pacific, lightning discharges, destruction of electronics in monitoring satellites, and an electromagnetic pulse that affected some power circuitry as far away as Hawaii.

The event was recorded worldwide as the plasma formed at least two intense equatorial tubes, artificial Van Allen belts, around the Earth [1], [2]. These tubes, or plasma toroids, contained relativistic electrons bound by magnetic fields; the source of intense amounts of synchrotron radiation. The radiation lasted far longer than expected; the decay constant was of the order of 100 days. (Mankind, unknowing, has viewed synchrotron radiation from the Crab nebula for centuries. The only known mechanism that produces synchrotron radiation are electrons spiraling about a magnetic field at nearly the speed of light).

Thus, the shape of the phenomena as recorded at radio, visible, and high frequencies was that of plasma "donuts" encircling the Earth, which mimicked the Van Allen belts.

Manuscript received May 19, 2003; revised October 15, 2003. This work was supported by the Mainwaring Foundation, in association with the University of Pennsylvania Museum of Archaeology and Anthropology, Philadelphia.

The author is with the Plasma Physics Group, Los Alamos National Laboratory, Los Alamos, NM 87545 USA (e-mail: alp@ lanl.gov).

Digital Object Identifier 10.1109/TPS.2003.820956

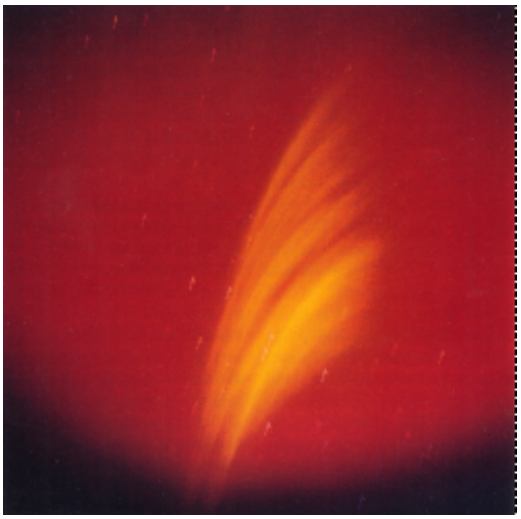

Fig. 1. Starfish thermonuclear detonation July 9, 1962, 400 km above Johnston Island. The photograph was taken from a Los Alamos KC-135 aircraft three minutes after initiation time. An artificial striated aurora has already formed from the plasma particles, spreading along the earth's magnetic field. The brightest background object (mark) at the top, left-hand corner, is the star antares, while the right-most object is θ-Centauri. The burst point is two-thirds of the way up from the lowest plasma striation.

The artificial aurora shown in Fig. 1 also shows plasma striations that arise from instabilities. This paper describes characteristic features of laboratory plasma experiments and simulations, especially for high-current Z-pinch conditions, and compares these features with petroglyphs and other ancient writings, which may have been associated with auroral observations.

As in the natural aurorae at the northern and southern magnetic poles, the streaming charged particle electrical currents, Birkeland currents, are of the order of megaamperes [3].

II. Dynamics of an Intense Aurora

The shape of the aurora is determined by the supersonic solar wind, Earth's magnetospheric shield (approximately 100 km above the Earth surface), and Earth's dipolar magnetic field. (It is the magnetopause that diverts the impingement of the solar flux into a tear-dropped shaped shell. At the widest, the width of the magnetopause is of the order of 130 000–150 000 km while the tail may stretch away from the Earth far beyond 1 000 000 km. For comparison, the mean distance between the Earth and Moon is 384 402 km).

The circular or oval inflowing and outflowing electrical currents are shown in Fig. 2. These sheets of electrical currents form the rapid waving curtains of light in an auroral display (Fig. 3), a result of the electrons interacting with and exciting molecules

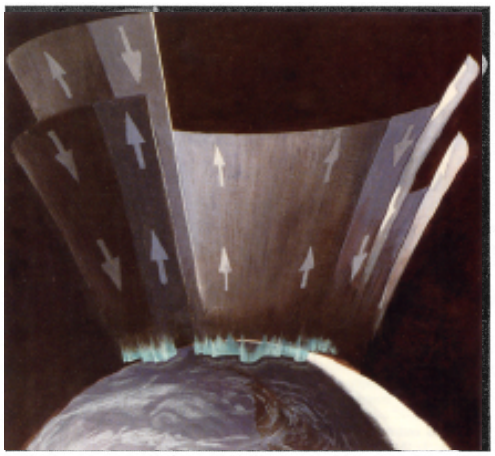

Fig. 2. Artists depiction of Birkeland currents flowing into and out of the earth's atmosphere at high latitude. These currents, once the subject of intense debate, are routinely measured by today's satellites and have total magnitudes of millions of amperes (megaamperes). Courtesy of S. G. Smith, Applied Physics Laboratory, The Johns Hopkins University.

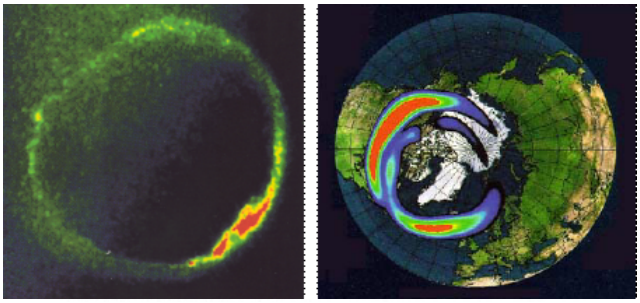

Fig. 3. (Left) View of the Earth's aurora obtained by UV light by the Viking satellite. The auroral emissions completely encircle the geomagnetic pole, located approximately in the center, and are brightest near midnight, located in the lower right corner. The diameter of this auroral ring is about 5000 km. (Right) The solar wind plasmas filtered through Earth's magnetosphere responsible for the aurora on Earth. These spectacular phenomena occur in two auroral arcs lying at polar latitudes in both the northern and southern hemispheres, and are caused by plasma electrons flowing down in sheets along the Earth's magnetic field. These sheets of electrons, or electrical currents, filament up to form the rapid waving curtains of light in an auroral display, a result of the electrons interacting with and exciting molecules in the upper atmosphere.

in the upper atmosphere [4], [5]. The aurora is sporadic, usually lasting for a maximum of several hours but sometimes for days. The most intense and largest auroral displays occur during a solar storm when the incoming flux increases dramatically [6].

III. Instability of the Auroral Sheets

A. Auroral Morphologies

The auroral plasma column is susceptible to two plasma instabilities; hollowing of the relativistic electron beam to form the sheets and the diocotron instability that cause the sheets to filament into individual current strands causing the "swirls" or "curtains" [7], [8]. These instabilities also produce the radiation observed over a wide range of the electromagnetic spectrum [9]–[11].

The dimensions of the auroral circle can be hundreds of kilometers in diameter while the width of the sheet can be tens of kilometers.

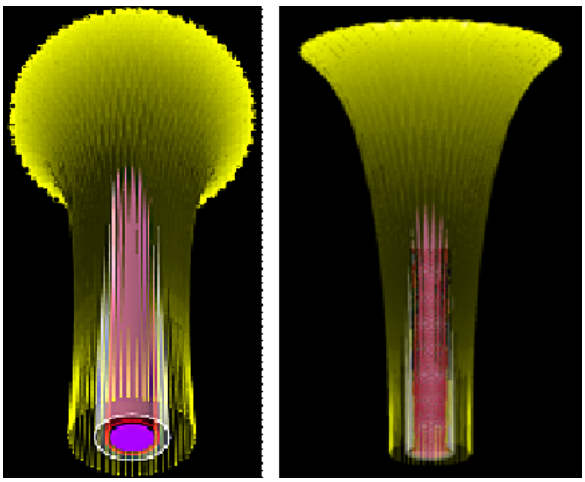

Fig. 4. Depiction of an intense auroral funnel. The figures show both down-flowing and up-flowing Birkeland currents contained with two Concentric sheets. (Left) Oblique upward view. (Right) Side view. Barely discernible at the lower center are the Z-pinch instabilities.

For an intense inflow of plasma, the aurora would be shaped by the strength of its own azimuthal magnetic field, i.e., a Z-pinch.

In the case of a strong aurora involving many tens of megaamperes of current, most of the funnel would be visible in light emission and the individual filaments and vortices strongly visible. In a narrow field-of-view, the light-emitting filaments would appear as "dots" or "elongated dots" and filamentary strands. This geometry would predominate if the charged particle outflow from the sun were to increase an order of magnitude or more for an appreciable length of time.[1] In addition, portions of the magnetosphere and its tail would also be visible [12].

Fig. 4 is a graphic depiction of an intense auroral funnel. The thin outer plasma has filamented into small diameter plasma currents and inner plasma sheets and core. The upper part of the funnel has either a diamond, mottled, or cellular structure, while the incoming part of the funnel consists (looking up) of concentrics of dots and cylinders. The instabilities that occur in the mid to bottom part of the funnel will be a topic of study in this paper.

For an intense aurora, the converging filaments are seen not only as dots, but also as dots connected to the visible converging filaments at higher altitude. We shall delineate the aurora plasma sheet into two parts, the upper funnel or inflow region and the lower plasma sheet and solid columns.

B. Auroral Luminance

Charged particle excitation from the inflowing plasma is responsible for the luminosity and color of atmospheric auroras. The color depends on the upper atmosphere's state and height above the Earth. Various deexcitation processes in atoms of oxygen and nitrogen cause mostly green, red, and blue auroras. Exceptionally yellow auroras can be observed in places where red and green auroras overlap. The most common green color is caused by the emission line 557.7 nm of the oxygen O(1S) [3].

[1]An increased outflow of plasma from the Sun in the past was first suggested three decades ago by Gold [70].

The luminance of auroras ranges from 4.83×10^{-5} lm per sterradian per meter square to 4.83×10^{-2} lm per sterradian per meter squared. In comparison, the full moon luminance is 6000 lm per sterradian per meter square.

Observations suggest that the geomagnetic storm producing an energetic aurora derives from the direct injection of 10 eV–10 KeV electrons from the solar plasma flux. In fact, the source of the high-energy electrons need not necessarily be solar but may be any electric space phenomena that causes an inflow of plasma to the Earth.

An update of research in solar plasma, interaction of solar and the Earth's space plasmas, geomagnetic storms, substorms, and aurorae, the magnetosphere and ionosphere, and the simulation of space weather may be found in [13].

IV. Experimental and Analytical Methodology

The experimental data was taken from various terawatt power machines with a majority of the data taken by the author on the Maxwell Laboratories Blackjack 5 pulsed-power generator. Data was also drawn from the U.S. Department of Energy Laboratories pulsed-power facilities at the Los Alamos National Laboratory and Sandia National Laboratories [14]. High-explosive generators in the U.S. and Russia added to the data set. The currents ranged from hundreds of kiloamperes to 150 MA and time scales from tens of nanoseconds to microseconds [15], [16].

The plasma load geometries were generated by applying high-voltage pulses to gas-puffs to simulate an aurora-like plasma inflow, wire arrays to simulate filamentation dynamics, and concentric plasma sheets formed by nested cylindrical foils to produce high velocity shock waves [17], [18]. In size, the geometries were a few centimeters in diameter and 2–3 cm in length. Thicknesses of the wires and foils were typically 10–30 μm.

A. Diagnostics

The diagnostics generally included laser shadowgraphy, Schlieren photography, laser-double pulse holography, fast framing cameras, streak cameras, X-ray detectors, bolometers, soft and hard X-ray pinhole cameras, Rogowski coils, and waveform recording probes.

In some experiments, thermoluminescent detectors measured the photon spectrum over 1–10 MeV, electron energy spectra, bremsstrahlung spectrum, and their angular distribution.

B. Solution of the Chandrasekhar–Fermi Equations on High-Performance Computers

Theoretical and computational analysis of a plasma column are based on a fundamental plasma theorem for conditions of dynamical stability. This theorem was first used in magnetohydrodynamics (MHD) by Chandrasekhar and Fermi to establish the condition for dynamic stability of cosmic gravitational masses balanced by gravitational, magnetic, and kinetic pressures [19]. The basic geometry under consideration by Chandrasekhar and Fermi was cylindrical as was that of Shafranov, who extended the use of the theorem to investigate equilibrium conditions for current-carrying plasma columns [20].

Extension of the theory to account for three-dimensional (3-D) kinetic motions were carried out by Peratt, Green, and Nielsen, who benchmarked the computations against both low- and high-current plasma columns with 3-D relativistic particle codes [21], [22]. (See also Section XVIII).

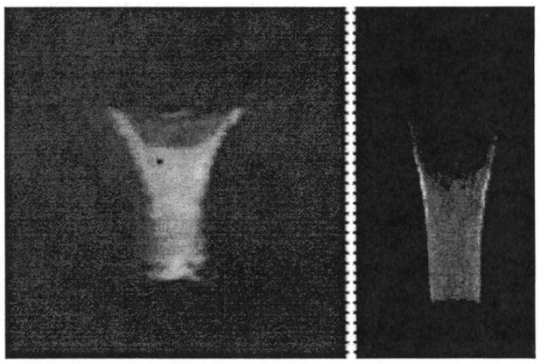

Fig. 5. Conical inflow of a current conducting plasma column. The flow is from top to bottom with striations in the body of the column, and the beginning of a plasma feature at top-center. These experimental photographs pertain to a 5 MV, 3 MA plasma.

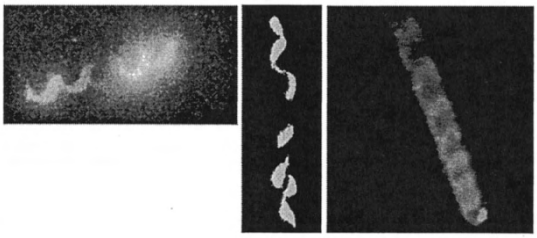

Fig. 6. Helical instabilities in the laboratory and space. (Left) 1.3-MA plasma column. (Middle) Centimeter-length plasma column conducting 2 MA. Framing camera picture, 5 ns (5 billionths of a second). (Right) Ten-kilometer, 150-mA electron current injected approximately 100 km above the earth.

Verification and validation of the computer codes are a necessity [23]. All simulations are benchmarked to high-energy density data. Similarly, experimental data are benchmarked to the simulations to understand the column evolution.

V. Evolution of the High-Current Z-Pinch

The overall time history of the pinched column, from formation to eventual breakup, has been a topic of some interest. The evolution is studied with the 3-D, electromagnetic and relativistic particle in cell simulation code TRISTAN [8], [24]. Other works on the topic are found in the literature [25]–[28].

Overall, the data give a picture similar to that shown in Fig. 4 where inflowing plasma converges into a striated or patterned plasma column (Fig. 5).

A. Instability of a Solid Plasma Column

A solid plasma column such as that shown in the center of Fig. 4 (or the lower column of Fig. 5) is susceptible to two types of instabilities, $m = 0$ (sausage) and $m = 1$ (helix), where m is the number of azimuthal variations, $\exp(m\vartheta)$ [8], [20]–[23].

The $m = 1$, or helix, is a common instability in both laboratory and space plasmas and occurs when a magnetic field axial to the column preexists. (It is not unusual for a plasma to produce a circular magnetic field with a slight vertical component that rapidly develops into the axial field needed for the development of a helix). Fig. 6 shows examples of both cases, respectively.

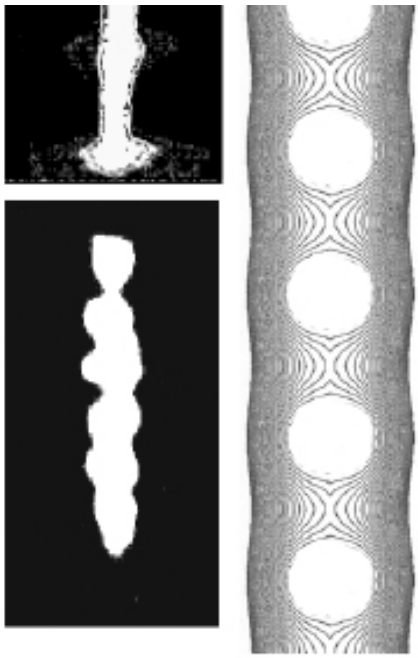

Fig. 7. Outer spheroids produced by the plasma pinch. (Top Left) Experimental, early time. (Bottom Left) Later time. (Right) MHD supercomputer graphical solution of the Chandraskhar–Fermi equations.

From left to right: a 1.3 MA plasma; a 5-ns 3-cm-long 2-MA plasma and a millisecond 150-milliampere beam, about 10 km long. Increasing the current in all cases produces a smaller diameter helix.

B. Column Structure

The morphology of the Z-pinch as it evolves in time is that of a self organizing structure of an outer spheroidal plasma envelope and inner toroids, as discussed by Ortiz-Tapia and Kubes [29], [30].

Generally, in an intense electrical discharge in the multimegavolt, multimegaampere range, as would be measured in an intense aurora, nine distinct pinches that are spheroidal in shape are formed. While there is no known theoretical basis for nine spheroids, experimentalists most often mention "between eight and ten." In Fig. 7, the bottom two were cut off in the recording. These spheroids, or "plasmoids" consist of an outer spheroidal plasma envelope and inner toroids that define both the magnetic fields and the currents within them [8].

1) Spheroids: The frames in Fig. 7 portray the outer spheroid isophotes, some including the central visible core (the central plasma core is not plotted in the simulation). The pictures on the left are X-radiographs while that on the right is a computer simulation. Generally, one, two, or three plasmoids are visible at a time but as many as eight are common. It is also not unusual to find a truncation or modification of the top-most spheroid.

2) Inner Toroids: Intense optical radiation, synchrotron radiation, and X-rays are recorded from the inner plasma toroids. The basic geometry is shown in Fig. 8, where (a) is the basic geometry, (b) is a framing camera picture of the centimeter size 1.3-MA pinch [29], (c) is the centimeter-size 6-MA pinch, and (d) is the centimeter-size 6-MA pinch with optically dense (brightest) plasma shown. Note that the densest plasma forms

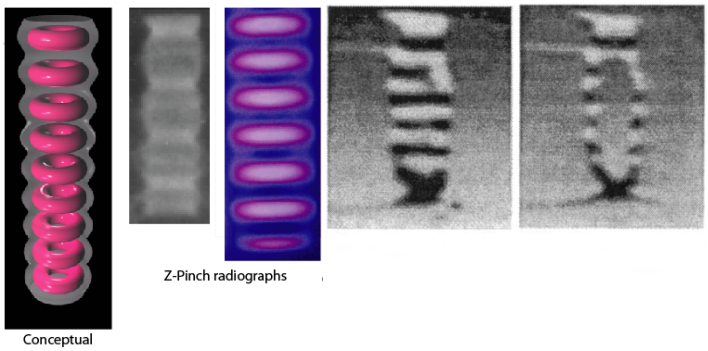

Fig. 8. Inner toroids within the stack of spheroids produced in a multimegaampere plasma column. (a) Basic geometry. (b) Centimeter-size 1.3-MA pinch. (c) Centimeter-size 6-MA pinch. (d) Centimeter-size 6–MA pinch with optically dense (brightest) plasma shown.

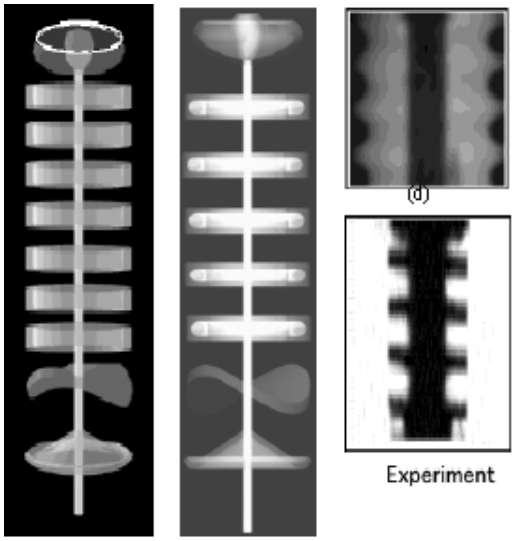

Fig. 9. (Left) Illustrations of simulations of the flattening of a stack of multimegaampere conducting plasma toroids. The current causes the toroids to both flatten out in the center and start to warp and fold at the ends as shown. (Right) X-ray radiograph of a l6-MA pinched plasma 4 cm in diameter. (Top) Plasma sinusoidal pinch perturbation at 6.5 μs. (Bottom) Formation of flattened toroids from the initial ripples at 9.5 μs. The bottom figure rungs appear cutoff, but are the natural shape. (Los Alamos Plasma Physics, P-24).

the top feature, the sides of the toroids, and the bottom base that flares downwards and away from the column.

VI. Evolution of the Plasma Column Toroids

In pairs, the electromagnetic forces on the toroids in the stacks shown in Fig. 8 are long-range attractive, short-range repulsive, or force-free (merging) [31]–[33]. However, in a stack, the repulsive-attractive forces tend to flatten all but the top and bottom toroids. This is illustrated on the left side of Fig. 9.

A pinched plasma X-ray radiograph is shown on the right side of Fig. 9. The top radiograph is a plasma column with sinusoidal pinch perturbation at early time. On the bottom, the radiograph shows that these ripples have rapidly converged inward by the intense self-magnetic pressure to produce flattened toroids.

The radiographs in Fig. 9 are sequential, measured in the X-ray regime at 6.5 and 9.5 μs after column formation. The total current conducted through a 4-cm column diameter was 16 MA. The bottom toroids appear to be cutoff photographically but this is the actual untouched radiograph.

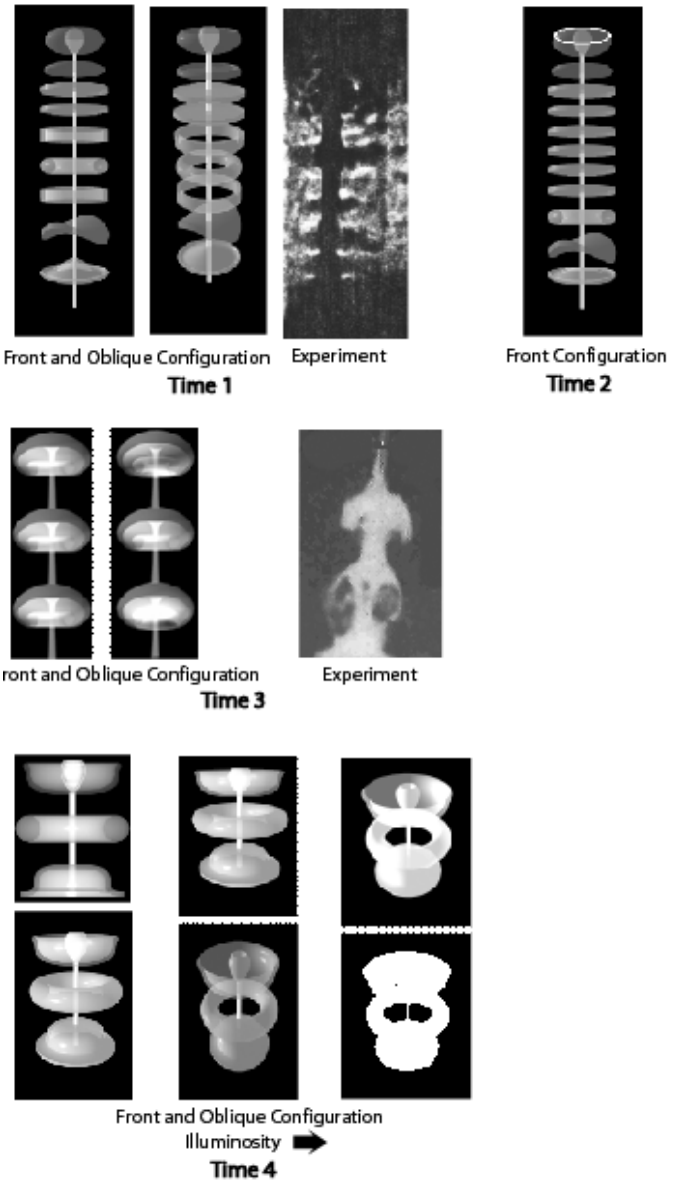

Fig. 10. Radiography derived time sequence of a multimegaampere stack of toroids in the highly nonlinear instability phase. The sequence shown starts from a previous nonlinear phase where the pinch ripples on the outer surface have collapsed into squared, folded and warped toroids. Figures derived from a few selected laser shadographs and schlieren photos. Time proceeds from left to right and top to bottom.

The experimental data set is a complete time-motion sequence of the Z-pinch. Selected radiography frames and simulation graphs have been assembled in Fig. 10, the latter of which is a time sequence of a multimegaampere stack of toroids in the highly nonlinear instability phase. Time proceeds from left to right and top to bottom. The current conducting plasma column shown starts from a previous nonlinear phase, where the pinch ripples on the outer surface have collapsed into squared, folded and warped toroids.

As shown in Time 1, the maximum number of toroids are those of the initial outer spheroid envelope, nine. However, as the current increases, the toroids come under intense self and neighboring toroid pressures forcing dramatic toroid deformations. In the data depicted, the top most toroid folds into a bulb-like shape.

Time 2 illustrates the flattening of all the toroids such as those shown in Fig. 9, bottom right.

With increasing current, the toroids warp violently and produce well defined vortex curls at their edges. These edge vortices wrap up in a spiral. In some case, the folding may be flat or square, as is the flattened toroid. The edges curl in and out and upwards and downwards to the current flow.

In some cases, mushroom-like structures form as shown in the center frames (Time 3). For increased current at later times, the center toroids are forced to merge, reducing their number as shown at Time 4. The central toroid can be tubular, flat, or spheroidal. Time 4 also illustrates the effect of luminosity on the morphology observed.

VII. Hydrodynamic Shockwave Patterns From Auroral Shocks and Colliding Plasma Sheets in the Upper Atmosphere

The auroral electrical circuit is by far the best known of all space plasma circuits [34], [35]. It is derived from a large number of measurements in the magnetosphere and ionosphere. Above the lower atmosphere, at about 100 km, multiple layers of plasma form the ionosphere. The auroras occur in the lower portion of the ionosphere, primarily from about 90 to about 150 km, as the result of electrons interacting with and exciting molecules in the upper atmosphere. Prehistoric man at northern latitudes often likened the patterns produced to the butting of goat's horns in combat [3].

The inflowing currents are relativistic (particles with velocities approaching the speed of light) and sporadic, producing high Mach number shocks at interfaces in the intense current plasma column (Fig. 4). In addition to the vertical particle flows are shock-surface phenomena produced by the impingement of the outer shell on the inner shell forming an extremely intense aurora when the outer shell stagnates at the main plasma column.

At early time a number of unperturbed surfaces exist that are susceptible to shock-induced instabilities, outlined by Zel'dovich and Razier [36]. For example, the outer cylinder surfaces shown in Fig. 4 eventually slam into the inner-cylinder surface whose inward acceleration has been stopped by the plasma it compressed.

Other planar surfaces susceptible to shock instabilities are the upper atmospheric strata. It is these layers in which we observe the auroral curtains and instabilities today from sporadic high-intensity electrical pulses traveling along the auroral column.

At a planar interface of gas or plasma, a shock pulse initiates a series of hydrodynamic instabilities that differ from the plasma column instabilities. In hydrodynamics, these are the Richtmeyer–Meshkov instabilities recorded by Budzinskii and Benjamin [37].

Initially, a pulsed perturbation on a denser layer causes a rippling of the layer that rapidly develops into periodically spaced spike like features. These features, or "spikes" then evolve in a way shown in the top frame of Fig. 11, the first frame of a laboratory simulation of the time evolution of an ionospheric layer shocked by a Mach 1.2 pulse (time increases from left to right and top to bottom) [38].

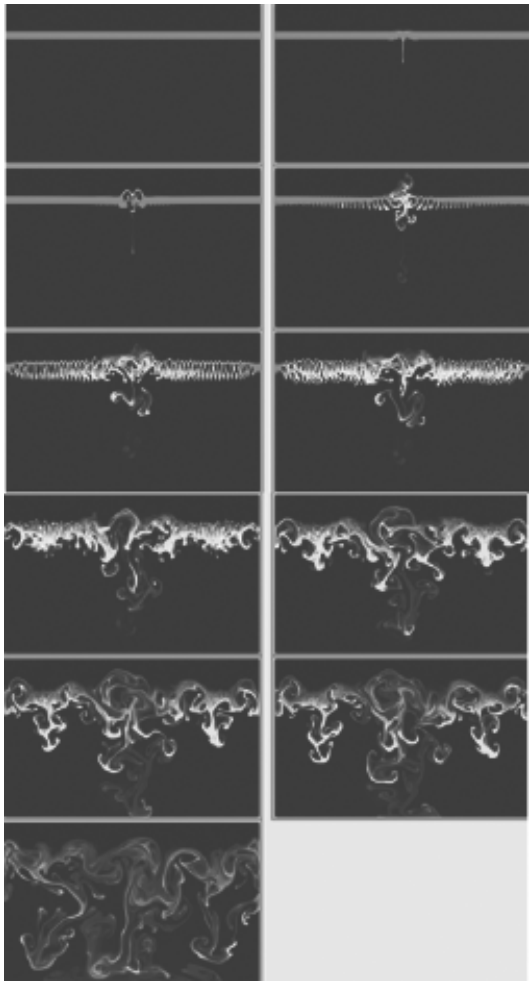

Fig. 11. Time evolution of an ionospheric layer shocked by Mach 1.2 pulse. Time increases from left to right and top to bottom. (RAGE calculation, R. Weaver, Los Alamos National Laboratory.)

As shown in the sequence, the shock impulse causes the generation of yet more instability spikes that themselves morph into yet more complex instability shapes. The center-most feature, the point of shock impact, has changed appreciably from its initial spike profile, into a tripling of morphology associated with fast instability growth [39].

VIII. Electrical Discharges Associated With Intense Auroral Currents

A. Lightning

Strong electrical discharges are associated with intense inflowing charged particles. This is the lightning most often seen in connection with atmospheric discharges whose tortuosity are the jagged and complex light strokes seen in the sky and accompanied by the sound of the shock wave.

B. Heteromacs

Kukushkin and Rantsev-Kartinov at the Kurchatov Institute, Moscow, Russia, found that, based on fractal dimension analysis of experimental data from plasma pinches, electric current-carrying plasmas are a random fractal medium. The basic building block of this medium was identified by Kukushkin and Rantsev-Kartinov to be an almost-closed helical filamentary plasma configuration called a heteromac [40].

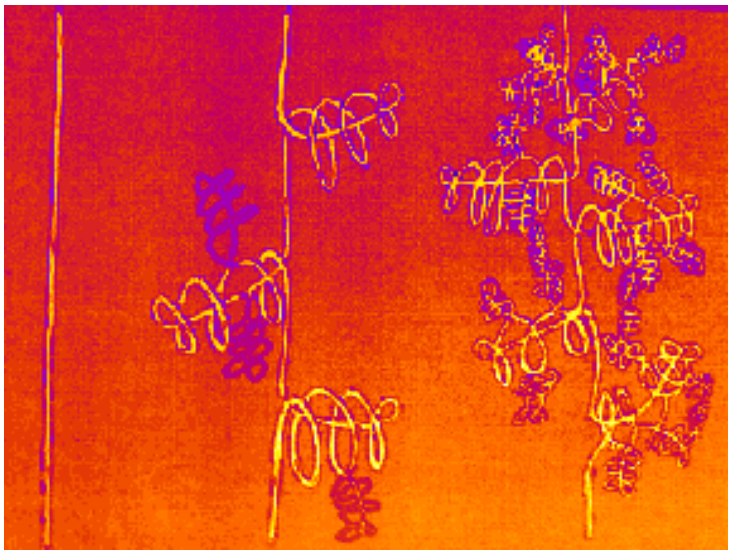

Heteromacs (Fig. 12) are coupled together through long-range self-sustained filamentation and, thus, form a dynamical percolating network with dissipation. Hence, heteromacs can include filamentary, cellular, and bubble-like clusters.

Heteromacs tend to repeat a pattern at increasingly smaller sizes in a random manner. The tendency of heteromacs is to display the plasma in random fractal, self-repeating and overlaying patterns.

IX. Petroglyphs

Petroglyphs, the carving of pictures on rock, have mystified and inspired historians, archaeologists, anthropologists, shamans, religious cults and even some astronomers for centuries, if not millennia [41]. They are found on every continent except Antarctica. Some are mere scratches while others were chiseled centimeters deep.

Petroglyphs, “rock art,” are thought to date back to the Pleistocene and Paleolithic—the earliest markings by man on rock. While the dating of petroglyphs has been a high priority for all who study or record them, there exists no consensus that an absolute age can be attached to any one pre-Colombian petroglyph.

Differing exposures to the elements leads to differing durability, coloration of the rocks patina or desert varnish (a natural coating of manganese, iron oxides, and clay minerals), and lichen overgrowth. The uncovering of the Glorieta Mesa and Rowe Mesa horizontal petroglyph sites from under one meter of earth near Santa Fe, NM might give the best indication of the ages of some petroglyphs. Campfire remnants some centimeters above the petroglyphs suggest that they are at least 4000 years old. In this paper, we shall limit the study to petroglyphs thought to range in age from 10 000 to 2000 BC [41].

A. von Humboldt pioneered the recognition of the social importance of information carried in petroglyphs. From 1799 to 1800, while exploring the hydrographic anomaly of the Casiquiare, a natural canal joining the Orinoco River of Venezuela with the Rio Negro of the Amazon basin, von Humboldt observed petroglyphs high on a bluff which prompted his advocacy that pre-Colombian civilization, far from being primitive, was the remnant of once-higher-societies in South America [42], [43].

Concurrent with Humboldt's exploration of South and Central America, Russia, and China, the Lewis and Clark expedition detailed their horticultural, geological, anthropological, and geographical findings of the American Northwest. On April 23, 1806, Lewis and Clark made their campsite on the Columbia River between Four O'clock Rapids to the east and John Day Bar to the west near what was named Hieroglyphic Rocks. According to Wilkes," about eight miles above their encampment they came to the Hieroglyphic Rocks. These are about twenty feet high, and on them are supposed to be recorded the deeds of some former tribe" [44].

Nearly 100 years later, Col. G. Mallory in an 1882–1883 report entitled "Pictographs of the North American Indians, A Preliminary Paper," voiced a much different opinion of petroglyphs [45]. In fact, the title of his later work is far too modest. "Picture Writing of the North American Indians" is probably the most comprehensive study of petroglyphs worldwide.

While the extent of Mallory's work is unparalleled, the interpretation of the phenomena is totally consistent with the regard in the late 1880s of the American West's perception of the "Indian" and other "primitive" peoples. For example, in the introduction to his work, Mallory paraphrases Sir F. Bacon in saying that "pictures are dumb history."

Mallory assigned various meanings to the petroglyphs that would be concordant with the beliefs of western settlers or Native Americans at that time. However, Mallory's interpretation of petroglyphs as thoughts of the mind is a concept that remains with us today.

His uneasiness with attributing this concept to petroglyphs is probably best illustrated by his statement, "the remarkable height of some petroglyphs has misled authors of good repute as well as savages. Petroglyphs frequently appear on the face of rocks at heights and under conditions which seemed to render their production impossible without the appliances of advanced civilization, a large outlay, and the exercise of unusual skill." Hence, like Humboldt, Mallory perhaps unconsciously subscribes to the idea that petroglyphs are other than primitive ritualistic scratchings [43].

X. Petroglyph Data

The data shown in this paper were taken from a data bank containing several tens of thousands of digital petroglyph photographs, many with their GPS longitude/latitude positions and orientation with respect to the most probable field-of-view.

In the American Southwest and Northwest, data was acquired by two teams of physicists, geophysicists, Bureau of Land Management employees, students, and petroglyph site stewards. Permission was obtained from both the U.S. Department of Energy and the U.S. Department of Defense to photograph petroglyph sites not accessible since 1943.

In situ investigations allowing direct digital recordings of the petroglyphs, notations of terrain and fields of view as well as global position satellite measurements were carried out in New Mexico, Texas, California, Utah, Arizona, Nevada, Colorado, Oregon, Idaho, Washington, and British Columbia, Canada.

Data from other known petroglyph-rich sites in the Midwestern and Northeastern U. S. was also included as was data from Loring and Loring, Thiel, Schaafsma, and Younkin [47]–[50].

The methodology included determining the most probable field-of-view, the position occupied, terrain or local obstacles, and degree of shelter most probably available to the artist. Special attention was given in this regard to work-intensive, deeply carved or precisely drawn petroglyphs (some, after carving, were then polished and painted). Other items of note were landslides, primarily of massive boulders partially covering petroglyph panels; panels whose faces had been partially cleaved by the elements, and boulders whose petroglyphs had been split by the cracking and separation of the rock itself. Access to sites of habitation and overall accessibility or inaccessibility to the petroglyphs completed the survey.

World-wide, most of the digital petroglyph data was acquired from the following places or countries and from regions adjoining them: Africa, Argentina, Arizona, Armenia, Afghanistan, Australia, Azerbaijan Bolivia, Borneo, Brazil, California, Canada, Canary Islands, Central America, Central Asia, Chile, China, Colorado, Columbia Dominican Republic, Easter Island, Ecuador, Egypt, England, Ethiopia, France, Germany, Gibraltar, Greece, Guiana, Hawaii, Idaho, India, Indonesia, Iraq, Ireland, Israel, Italy, Kashmir, Korea, Malta, Mexico, Macedonia, Malta, Minnesota, Mississippi Valley, Morocco, Namibia, Nevada, New Caledonia, New Guinea, New Mexico, Nicaragua, Norway, Okinawa, Oklahoma, Oregon, Pakistan, Panama, Paraguay, Pennsylvania, Peru, Portugal, Russia, Scotland, Siberia, South Africa, Spain, Sri Lanka, Sweden, Switzerland, Tahiti, Tibet, United Arab Emirates, Uruguay, Utah, Uzbekistan, Venezuela, Washington State, and Yemen.

Most of this data was contributed by individuals residing in or having collections of material from these regions [51], [52].

Finally, the data was cataloged according to morphology and plotted on 3-D computer renditions of scanned topographical maps. The results of this survey, entail the most probable field-of-view of the artist for differing petroglyph types and map the skewness inherent in the drawing. The data show that petroglyphs have a preferred orientation on a world wide basis and on morphology type, indicating that they are reproductions of plasma phenomena in space. These results will be presented in another report.

XI. Data Carried in Petroglyphs

Petroglyphs are images created on rock by means of carving or "pecking" the outer surface to expose the surface underneath. Most rock surfaces, independent of the chemical composition, are covered by a thin layer called a patina or varnish. This patina is created naturally by the rocks exposure to the elements. Rain, snow, sunlight, and extragalactic radiation such as gamma rays interact on the surface with salts and minerals, and even the crystalline structure of the rock, creating a thin outer darkening of the rock, a natural coating of clay minerals, manganese and iron oxides.

Prehistoric man would chisel or peck away the patina and expose the original stone surface to create the petroglyph image. Rock panels that derived from volcanic basalt flows are favored

Fig. 13. Petroglyph panel, Arizona, USA.

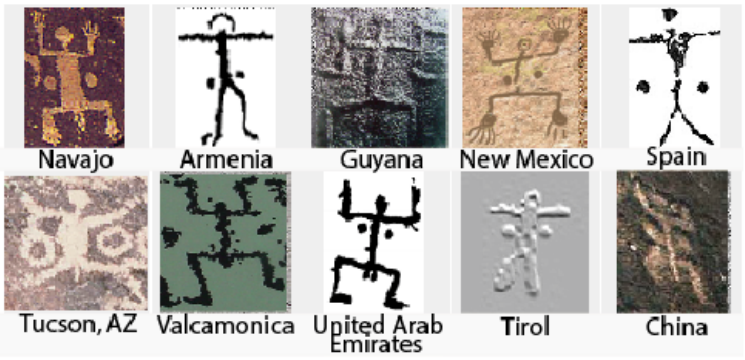

Fig. 14. Anthromorphic or man-like style of petroglyph named a "squatter." The illustrations shown are those of the rarer "double-dot" squatters; those having two dots on either side of the midsection. Left to right, top to bottom: Northern Arizona, Armenia, Guiana, New Mexico, Spain, Tucson Arizona, Tyrolian Alps, Italy, United Arab Emirates, and Venezuela.

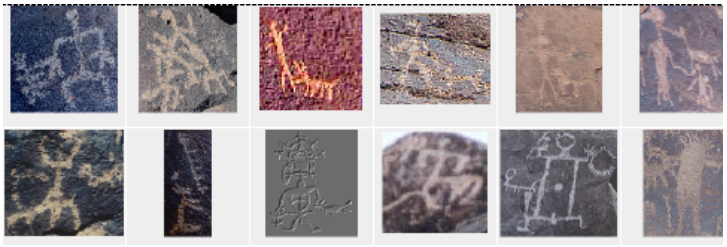

Fig. 15. Heteromac style petroglyphs (small sampling).

for petroglyph recordings. However, carvings in other materials were also used. A frequent way of recording was the use of "scratch petroglyphs" where scratches with a sharp stone were used to create patterns [50].

Pictographs that in this report are placed in the same category as petroglyphs, are made using paint instead of carving into the rock. Other objects from antiquity: statuettes, pottery, and structures are also placed in this category. Delineation will be presented in a following paper.

While single petroglyphs may be found, petroglyphs are most often found grouped in selected sites by the hundreds or thousands (Fig. 13). Sometimes the same rock facing has been overwritten two or three times. The appearance of such sites is one of random disarray of crudely drawn animals, people, unrecognizable anthromorphs, and abstract patterns or symbology. (A "rich cache" of petroglyphs consists of many hundreds or thousands of figures.)

Petroglyphs may be found in readily accessible places or in highly precipitous locations; in the open or within crevices. Generally, the discovery of one petroglyph results in the rapid spotting of dozens or hundreds more. This paper will suggest a rationale for petroglyphs being carved in difficult or specialized locations when equally satisfactory rocks in more readily accessible locations are in the vicinity; for example, the line-of-sight to the Earth's magnetic poles and highly conducting regions on the Earth's surface. These are the criteria of an intense aurora today: its appearance at the magnetic poles and the subsequent electrical damage to conduction paths such as the Alaskan oil pipeline [6].

A common image among petroglyphs is lightning-like discharge figures.

XII. Association of Petroglyphs With an Intense Aurora

The study of the aurora has been one of gathering as much information as possible about the influx of particles from space and its effect on Earth's space, plasma environment, and upper atmosphere. As such, the aurora is a stimulus to improved laboratory work on many different processes important to plasma physics. However the purpose of this paper is neither of these, but rather an attempt to explain how in man's prehistory recordings of high-energy-density phenomena (some not experimentally recorded until the last few years), could have been carved on rock in an accurate, systematic, and apparently temporally reliable fashion.

Eighty-four distinct high-energy-density Z-pinch categories have been identified in petroglyphs, nearly all of which belong to the archaic [50] class. Only a small percentage of these petroglyphs, or parts of petroglyph patterns, do not fall into any of these categories.

Fig. 14 shows ten examples of a single category of petroglyph found worldwide: an anthromorphic man with a dot on either side of the midsection. The anthromorphic man, with or without the side dots, called a "squatter" by rock art collectors, is recorded everywhere.

On large rock panels such as Fig. 13, overlaid petroglyphs are often heteromacs: figures with yet smaller figures attached, inside, or nearby. As the displayed figures in the sky evolved, perhaps over a decade, other overlays were added to represent the changes. Thus, association of petroglyph morphologies allows an epoch of electrical discharge evolution to be extracted from the carvings.

A very small sampling of petroglyphs drawn in the heteromac format is shown in Fig. 15.

A. Direct Comparison of Plasma Phenomena With Various Petroglyph Morphologies

Fig. 16 is a comparison of petroglyph images to both experimental and computational recordings of a plasma pinch. The frames on the left are radiographs of the pinch, the middle frame is a high-fidelity computer simulation of a plasma pinch, while the images on the right are a selection of petroglyphs typical of this morphology.

In the visible, the central plasmoid stack or parts of it would be observable dependent upon both the location of the observer

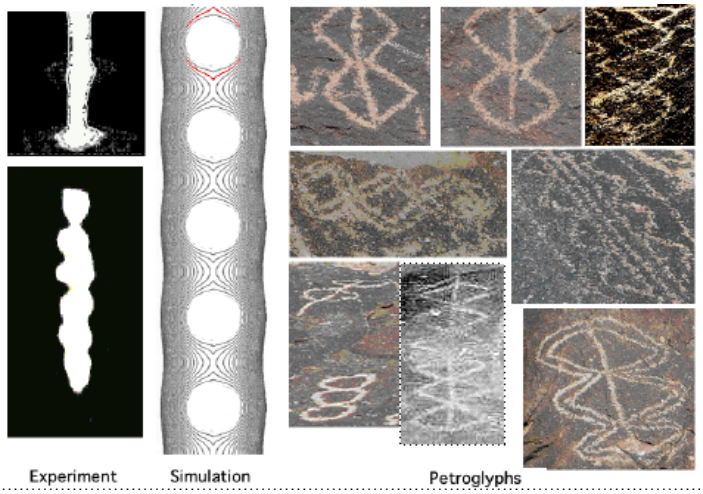

Fig. 16. Pinch instability characteristics of a plasma column. (Left) Plasma light photographs, early time. (Middle) Graphical solution of the Chandasekhar–Fermi equations. (Right) Petroglyphs. The patterns are found world-wide.

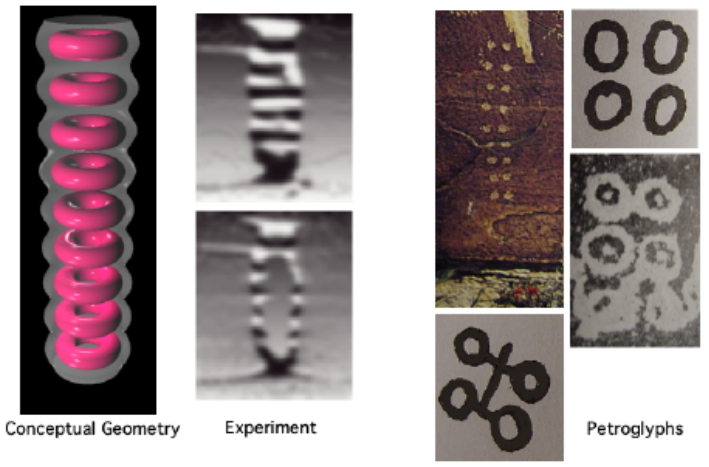

Fig. 17. Conceptual geometry of a stack of nine plasmoids produced in a high-current plasma column. (Left) Experimental and conceptual data of a stack of toroids along the pinched plasma column. (Right) Petroglyphs depicting stacked toroids. Note that the double row of dots numbers nine, the exact number of toroids generally produced in a plasma pinch.

and the duration and location of a current pulse propagating along the column. Because of the time required to produce certain classes of morphologies of petroglyphs and also the precipitousness of location, we conclude that petroglyphs were produced during daylight conditions, perhaps twilight or dawn. This then allows an estimate of the luminance necessary to see auroral plasma phenomena.

1) Spheroids: The petroglyphs in Fig. 16 accurately portray the outer spheroid isophotes, some including the central visible core (the central plasma core is not mapped in the simulation). Generally, one, two, or three plasmoids were visible at a time but as many as eight are common. It is also not unusual to find a truncation or modification of the top-most spheroid.

2) Inner Toroids and Surrounding Features: A more impressive sight than the outer spheroid shell would have been the intense optical radiation from the inner plasma toroids shown in Fig. 17.

The petroglyphs to the right Fig. 17 are typical of those commonly found in a stack of circles. One of the petroglyphs has captured the optical radiation from all nine toroids.

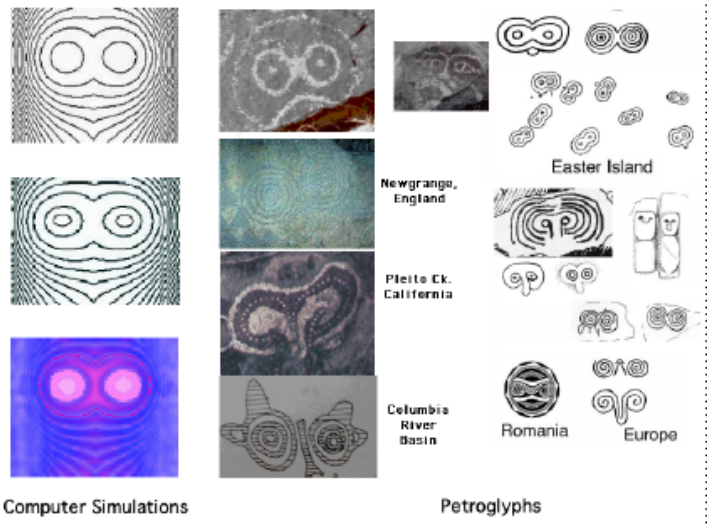

Fig. 18. Eye and nose masks. (Left) Isophotes from a portion of the graphical solution of the Chandrasekhar–Fermi equations. (Right) Eye mask and prominent nose petroglyphs.

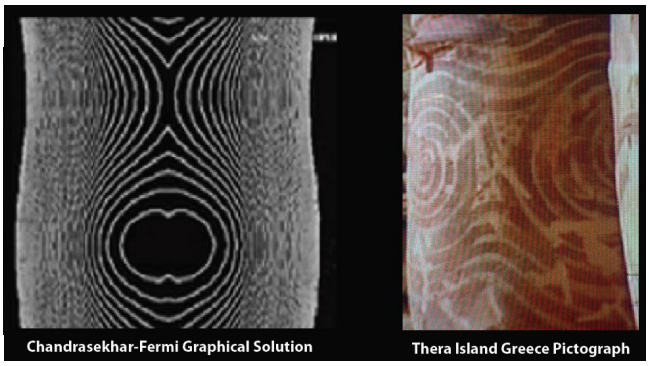

Fig. 19. Face masks as collected from various locations on Earth. The figure at the top left is a portion of the graphical solution of the Chandrasekhar–Fermi equations.

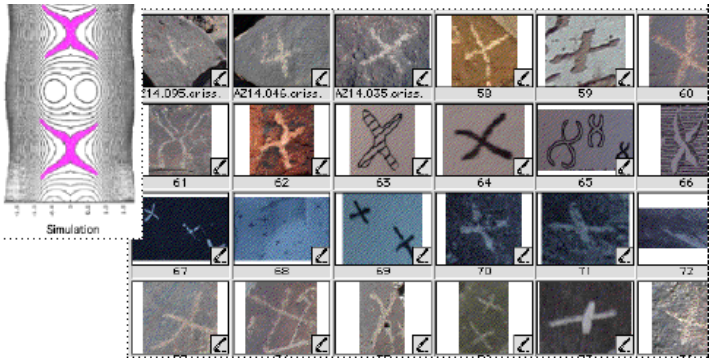

Fig. 20. Separatrix magnetic field merging crisscrosses. (Left) Portion of the graphical solution of the Chandrasekhar–Fermi equations.(Right) Assortment of petroglyph criss-crosses.

The middle isophotes reveal more detail. A totally unexpected feature appeared when the isophotes were artificially colored: "nose" and "eye brow" features. These features are shown in Fig. 18, the so-called petroglyph "eye masks" and Fig. 19, the "face masks."

3) The Separatrix "X" Points: An appreciable number of petroglyphs have captured the separatrix pattern between plasmoids with rather high fidelity (Fig. 20). (The "script-like" X separatrix should not be confused with the well-defined, circle-enclosed, square-cross petroglyph.)

Fig. 21. Separatrix Patterns as collected from various locations on Earth. The figure at the upper left is a portion of the graphical solution of the Chandrasekhar–Fermi equations.

The complete patterns containing the X-type separatrix are shown in Fig. 21 as numerically generated from the Chandrasekhar–Fermi equations for a plasma column. The diversity of cultures preserving common rock art themes is apparent in the separatrix patterns.

XIII. Evolution of a Columnar Stack of Plasma Toroids

In rock-art terminology, the experimental images shown on the right side of Fig. 9 would be classified as a "caterpillar" and a "ladder." These are reproduced again in Fig. 22. The sequences shown correspond to the rise-time portion of a long current pulse, that it, increasing electrical current.

A. "Caterpillars" and "Ladders"

Fig. 22 shows the experimentally reproduced conceptual geometry. The inner toroids have been flattened while the upper most toroid has folded inward, like the closing of a petal of a flower, into an oblong shaped object. The second uppermost toroid is also starting to fold upward. The increasing current has also started the warping of the flattened toroids as well as forming a cone shaped toroid. Fig. 22(c) and (d) show the X-ray radiographs of the experimental plasma. The analogous petroglyph recordings, the well-known caterpillar and ladder are shown to the far right.

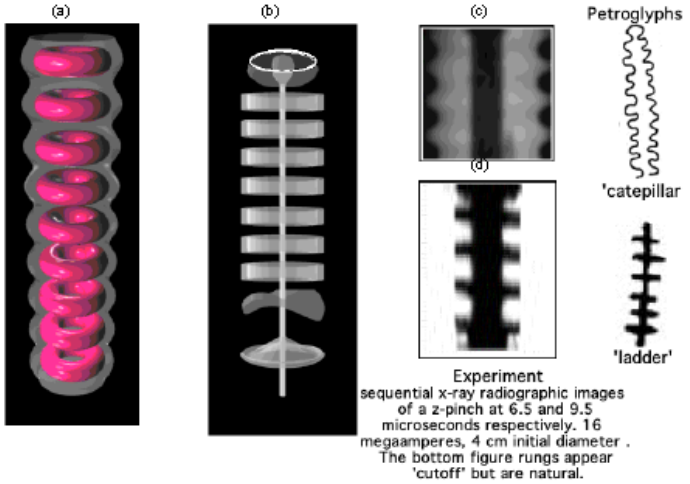

Fig. 22. (a) and (b) Conceptual geometries of a stack of multimegaampere current conducting plasma toroids. The current is increasing from left to tight, causing the toroids to both flatten out in the center and start to warp and fold at the ends as shown in (b). (c) Initial plasma sinusoidal pinch perturbation. (d) TPSO 136 2 late-time 16-MA current induced plasma ladder. The corresponding petroglyphs analogies are shown to the far right.

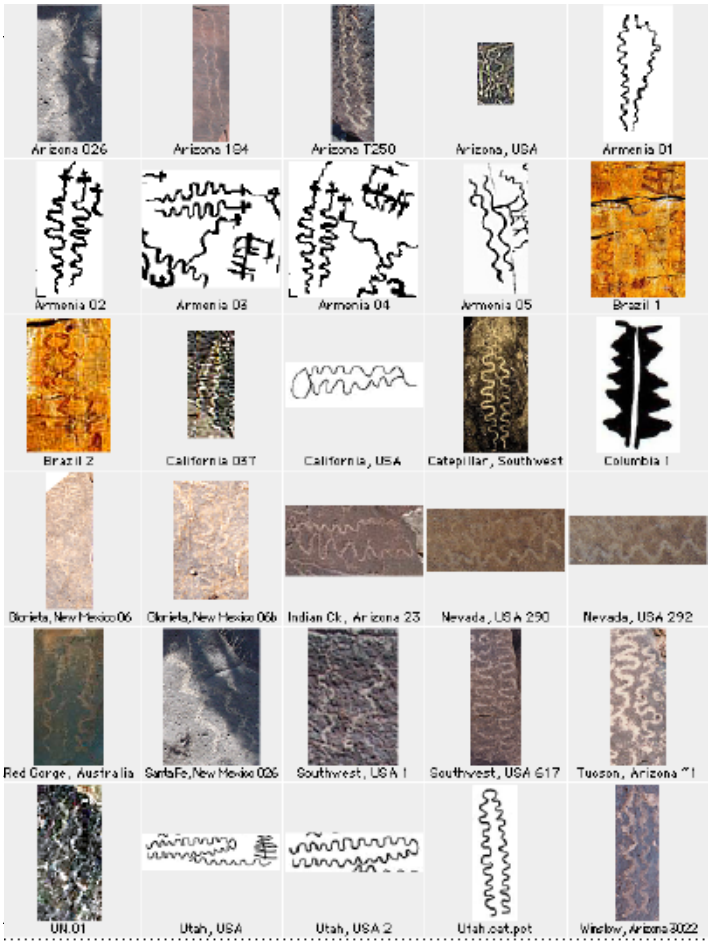

Fig. 23. Collection of caterpillar category petroglyphs.

Figs. 23–25 are a collection of caterpillar and ladder category petroglyphs found worldwide. It is meaningful that caterpillars and ladders are found in association.

Where the toroid stack consists of both spheroidal and flattened toroids, the optical radiation is brightest where the plasma is densest, i.e., closest to the edges of the toroids. This leads to a less well-known but still common petroglyph known as a

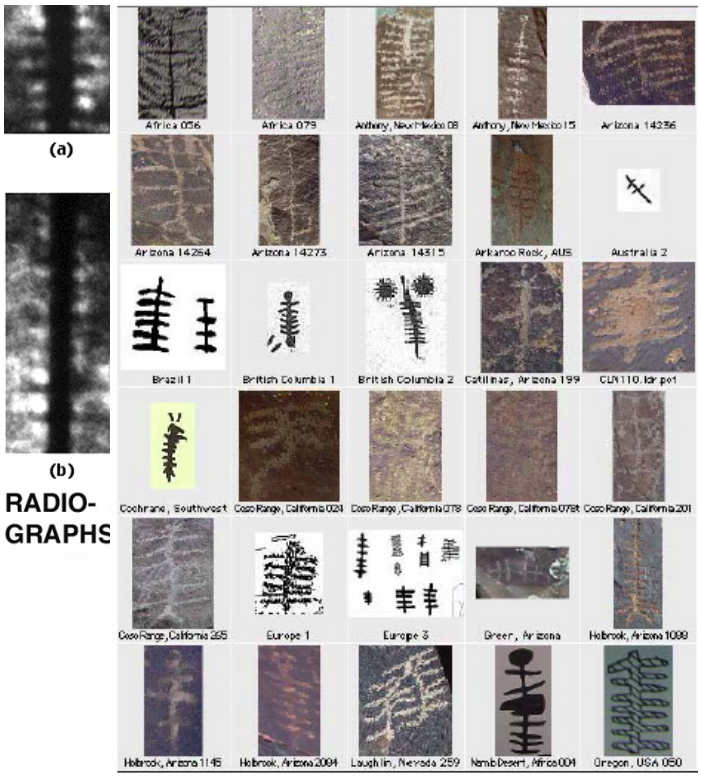

Fig. 24. (Left) Laser shadowgrams of plasma instabilities. (a) Stack of flattened toroids. (b) Later time shadowgram. The tips of the flattened toroids have started to curl in and form vortices. (Right) Collection of ladder category petroglyphs.

Fig. 25. Collection of ladder category petroglyphs (continued).

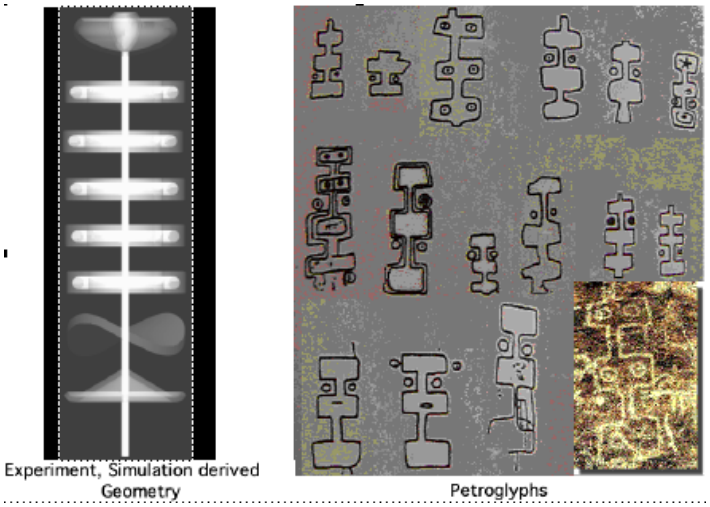

Fig. 26. (Left) Morphology and radiation properties of a stack of toroids beginning to undergo intense pressures from neighboring toroids. (Right) Pipette petroglyphs.

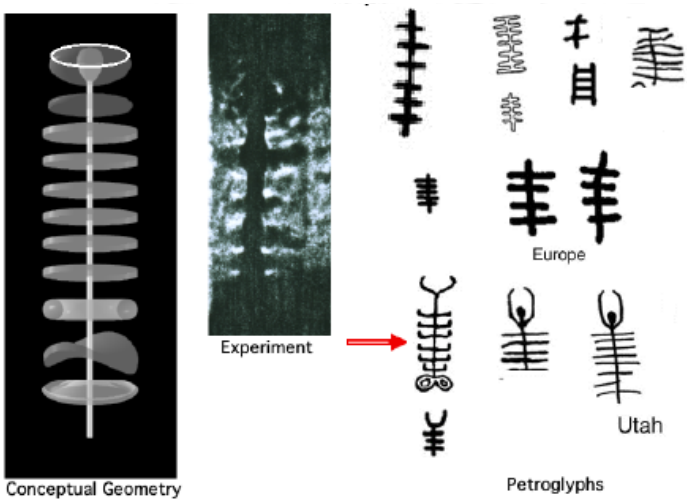

Fig. 27. (Left) Conceptual geometry and experimental laser shadowgraph of an intense current-conducting toroidal stack.

"pipette" (Fig. 26). The pipettes shown in Fig. 26 all have symmetrical pairs of "eyes." However, many petroglyphs simply show the outline of a pipette without any indication of hot spots or "eyes."

Experimental and petroglyph representations of these nonliner column instability morphologies described in Fig. 10 are shown in Fig. 27.

The petroglyph carvers have managed to capture all of the phases of the Z-pinch instability seen in the laboratory. These phases include the ladder and enclosed ellipsoidal top-most toroids. Some show the eyes of the bottom spheroidal toroids yet to be affected by the currents of the neighboring toroids.

Perhaps the most important feature depicted in the petroglyphs shown in Fig. 27 is the curling of the edges of the flattened toroids. This feature is exact enough so that a time-motion representation of the curling can be made and directly compared to its experimental counterpart. The curling or folding progression thus provides time information when the petroglyphs are scaled to laboratory data. [The time scaling will be given in another paper].

B. Vortices

With increasing current the tips of the "ladder rungs" begin to curl and form a vortex. With yet a stronger current, the toroids themselves roll up as shown in Fig. 28.

Fig. 28 provides the first direct evidence of the exactness to which petroglyphs were carved in spite of cultural influences in interpretation. The ladder rungs (stacked medium current toroids) are shown to fold and bend as do the laboratory photographs. Subtle changes in the petroglyphs corresponding to the plasma instability morphologies have been reproduced with precise accuracy, even including, in proper order, the admixture of toroid types.

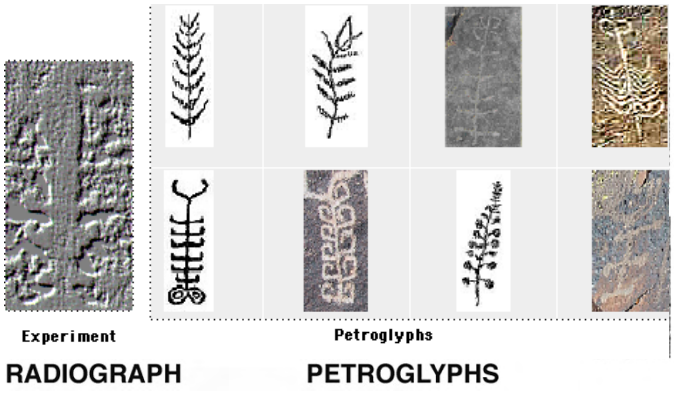

Fig. 28. (Left) Laser back-illuminated plasma pinch. The photograph has been digitally stratified to bring out the curling of the edges of the bottom, flattened toroids. The cathode is at the top. (Right) Sample collection of petroglyphs showing the transition from the ladder phase of the instability to toroid vortices. (Left to right, top to bottom). The examples shown have been collected from several parts of the world.

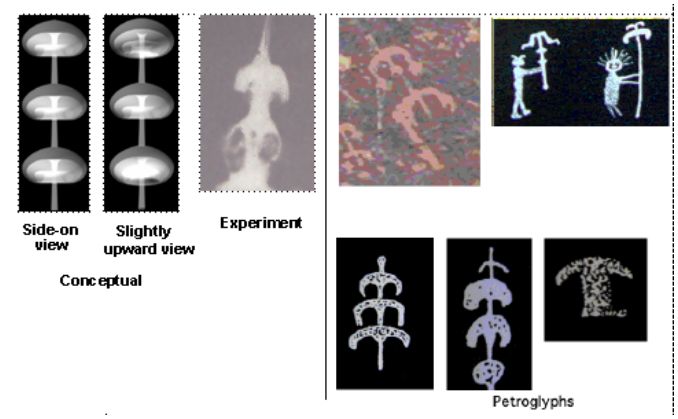

Fig. 29. (Left) Vortex formation in sub and multimegaampere pinched plasma columns. (Right) Petroglyphs.

In all cases, the top-most toroid, the terminus in an electrical discharge, is indeed at the top of the petroglyphs and shows the transition of the pincher type shape associated with the so-called scorpion petroglyphs into a folded petal as the top toroids fold up and close on themselves. Likewise, the slight upward bend of a flattened toroid at the middle of the column, its eventual curling at the end of the toroid, and the nearly-square vortex folding into knots has been accurately portrayed. The accuracy of these MHD instabilities suggests that an appreciable amount of time of a particular morphology was visible to the petroglyph carvers.

C. Intense Current Vortex Deformation

Further along the current rise, the vortices morph into a variety of cupular or cone shapes. Fig. 29 shows experimental and petroglyph recordings of this phenomena. The downwardly shaped cup figures, or "mushrooms," are a common theme in petroglyphs. The frames on the left are radiographs or radiograph derived data while those on the right are petroglyphs.

XIV. Universality of the Basic Plasma Instability

If an intense aurora were the source for unusual bright objects seen in the nighttime sky, these objects would have been observed worldwide. What would be observed depends on a number of physical properties of the auroral funnel, Fig. 4, and the current-carrying magnetosphere tail. These include the intensity of the current producing the instability, the intensity and

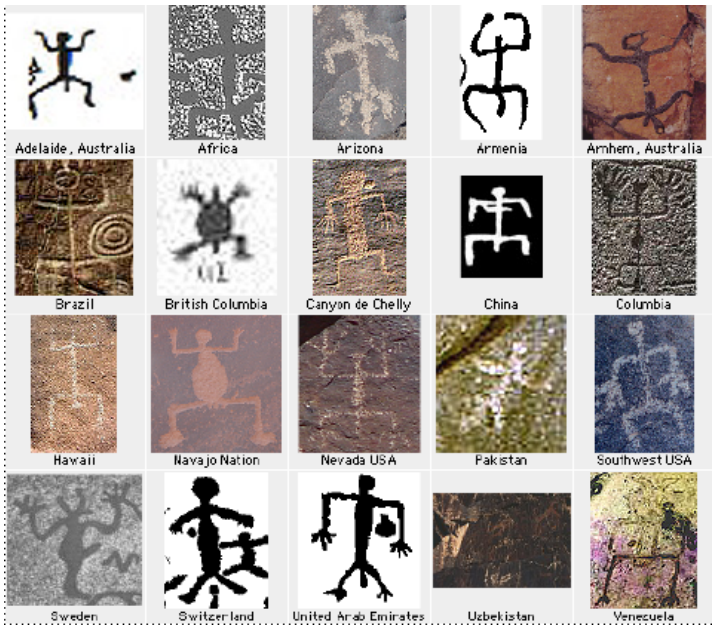

Fig. 30. Commonality of the most often depicted petroglyph, the squatter human or anthromorph.

duration of sporadic current pulses within the auroral plasma column, and the orientation of a column undergoing nonazimuthally symmetric motions.

While the previous figures have suggested that the phenomena was universally seen, what could be observed would depend on the observer's location on Earth and whether or not the entire column was visible or illuminated, or some portion of it, as in auroral displays today.

Fig. 30 is a collection of one of the common petroglyphs encountered in the field: the squatter. It is usually interpreted as a human figure or anthromorph with squatting-like legs and either upturned or down-turned, or mixed, arms. It is unfortunate that this one morphology has been interpreted in modern times as representing a human or an anthromorph. As such it is widely ignored in favor of more exotic and realistic petroglyphs forms. Perhaps for this reason, petroglyphs have been viewed as dumb history.

In reality, the forms shown in Fig. 30 mimic closely phenomena associated with the highest energy releases known, some of whose instability shapes were not known even a few years ago. Fig. 30 also shows that this basic shape was recorded independently of cultural bias or embellishment found on other petroglyphs.

The anthromorphs shown in Fig. 30 have several variations: the basic squatter depicted; the squatter with a bar or belly at the midsection; the squatter with either one or two dots on either side of the midsection; the squatter with two dots around the anthromorphic head, often drawn as extended ears; and the extension of the basic shape to reptiles, etc. The extremities may be upturned, down-turned, mixed; sometimes shown with three digit fingers or toes.

There is perhaps no way of estimating how often this figure occurs; carved, pecked, or scratched on rock. It may have existed in inestimable numbers. The remainder of this section investigates the variations associated with the basic shape and why this is the basic instability shape.

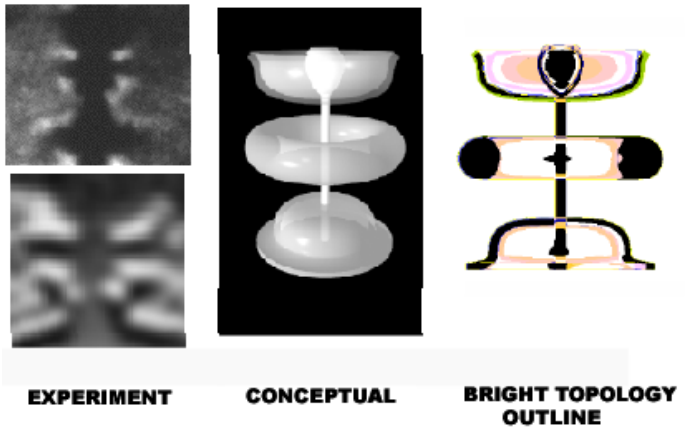

Fig. 31. (Left) Plasma instability profiles for a pulse illuminated section of a plasma column. Laser shadowgrams. (Right) Experimental and simulation derived geometries for extreme plasma currents in a plasma column. The illumination is strongest where the plasma is dense, that is, along the edges of the figures below and the cross-section of the center toroid.

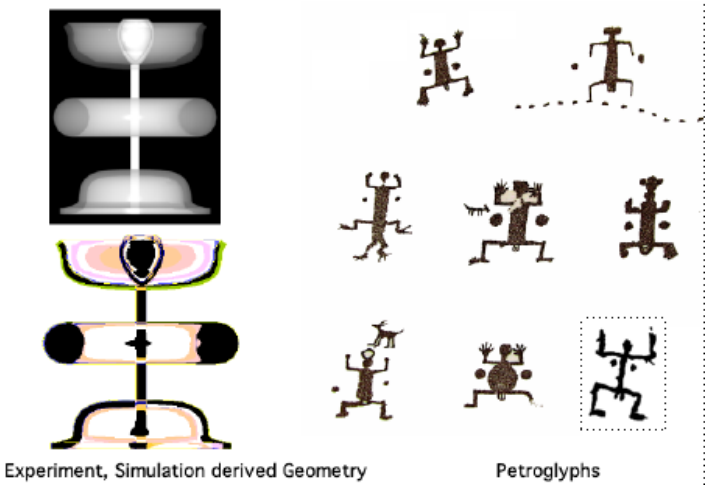

Fig. 32. (Left) Configuration and cross-sectional views of the intense current discharge. (Right) Petroglyphs. All are from the Western U.S. except the lower right figure that is from the United Arab Emirates.

A. Azimuthal Current Ring Structure Formation

In addition to the auroral plasma column instabilities, another well-known instability type occurs for intense currents having a slower rise-time. Because of the azimuthal currents and strong interactive forces, the flattened toroids merge to reduce the number of apparent toroids. The enclosed ellipsoidal top-most structure is present, but the central toroids combine to form a single azimuthal current carrying toroid. The geometry for this configuration is shown in Fig. 31.

In this case, the instability consists of a top electrode consisting of a few toroids that have folded and closed to produce a central bulb, an upward (or downward) cup, a central plasma toroid, and a bottom, usually downward turned toroidal cup.

Since it is an electrode, the cup torus at either end can take on a number of shapes. Usually the top electrode shows a variety of patterns. The patterns can be lightning-like, ellipsoidal, triangular (that can resemble the shape of a bird), a lightning bolt or multiple filament current terminations.

Fig. 32 shows a number of petroglyphs found globally that share this peculiar geometry. Another variation on the azimuthal current ring structure formation is petroglyphs that have symmetrical dot-like enhanced ear lobes or symmetrical dots at the lower extremity of the interpreted figure.

Fig. 33. (Left) Configuration and cross-sectional views of the intense current discharge as viewed obliquely to the plasma column. At times, two or more toroids are seen in line-of-sight emission. (Right) Petroglyphs.

The top image in Fig. 32 is the instability cross section. The bottom picture has been superposed with elements of the plasma instability. At the top of this figure, two toroids can be made out enclosing the central bulb. At midsection a toroid such as that shown in Fig. 32, but slightly warped, is seen. Beneath this is a highly flattened and warped toroid followed by the usual conical or cup bottom terminus as at the bottom of Fig. 31.

When viewed obliquely, the toroid is obvious and petroglyphs depicting the left side of Fig. 32 are omnipresent (Fig. 33). Note that the brightest plasma is at the edges except for the toroid, where denser and brighter plasma is innermost. At times, as the sporadic current pulse travels along the plasma column, one, two, or more toroids are seen in line-of-sight emission.

Fig. 34 shows yet another representation of this same class of petroglyph.

A different perspective of this same instability is shown on the left side of Fig. 35. In this case, the instability is shown at a somewhat later time when the central toroids have merged into the oblate shape at the center (the central feature can be accurately represented by a toroid; a flattened toroid, either tubular or warped; an ellipsoid, or no apparent toroid at all).

The visibility of the backside of the top cup is echoed in the petroglyphs that show the same shape around the central plasma bulb. Some show the central orb as either fully or partially enclosed.

B. Aurora Luminance

The luminance of a bright aurora today can be of the order of 5×10^{-2} lm per sterradian per meter square at 3–10 MA. However, a 16-MA current laboratory Z-pinch (Fig. 22), when scaled to a catastrophic aurora, could be expected to produce instabilities whose luminance varied in proportion to the current within the pinched column. For this case, the luminance might increase to 5 lm per sterradian per meter square, saturating the individual instability features as sporadic current pulses propagate along the column.

For these luminances, the plasma instability configurations shown in Fig. 33 would take on a new appearance such as depicted in Fig. 36. The plasma cups shown on the left of Fig. 36

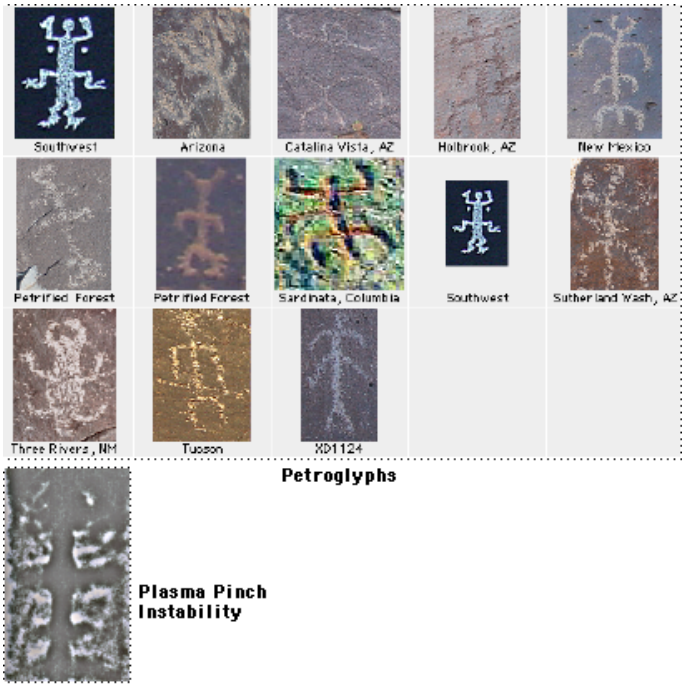

Fig. 34. (Bottom) Plasma pinch instability. When multikiloamperes or megaamperes of current flow though the plasma column, the flattened toroids both flatten and warp. (Top) Petroglyphs representative of the warping phenomena, for example, in the "belly" of the "squatter" men shown.

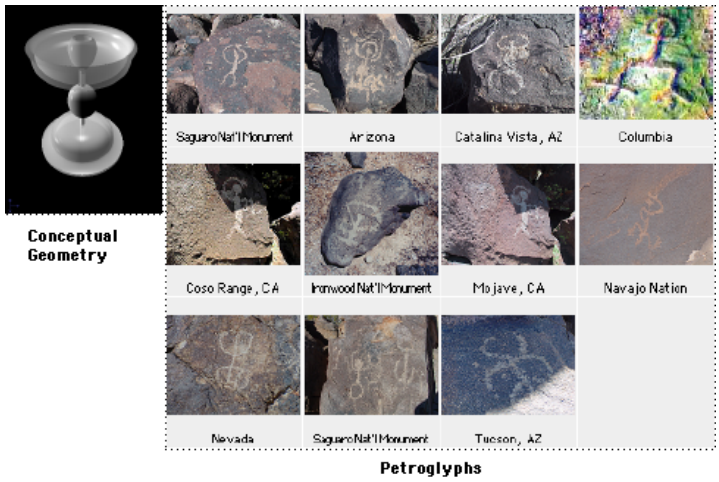

Fig. 35. (Left) View of the intense current discharge as viewed obliquely to the plasma column. (Right) Figures clearly depict the cup top-most terminus.

represent the top-most terminus of a column such as shown in Fig. 32. It is of interest to note that some of the petroglyphs on the right of Fig. 36 show an equivalence of a plasma trifurcation at the bottom of the figures.

C. Kokopelli

No description of petroglyphs would be complete without the mention of Kokopelli, the flute-playing figure that has inspired surprisingly, far-ranging folk-stories. With little cultural embellishments to the image, these are found world-wide.

Fig. 37 shows a collection of Kokopelli figures. At the top are two examples taken from a plasma discharge. These figures are respectively, early and late time photographs of the discharge. Whether or not the subjective interpretation of these

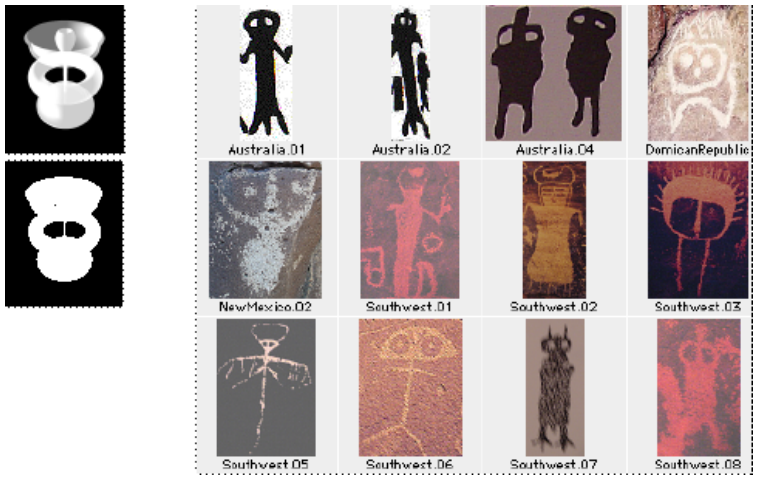

Fig. 36. (Left) Bright plasma instabilities, top to bottom, increasing luminance. (Right) Petroglyphs. Some show the entire body including the trifurcated base.

Fig. 37. Kokopelli. Examples from plasma discharges and world-wide interpretations on rock.

shapes would result in the small sample of petroglyphs shown below is left to the reader.

XV. Instabilities in the Upper Plasma Sheet and Their Correlation to Petroglyphs

The polar cap and magnetospheric cusp regions are roughly conical in shape as the inflowing solar wind flows down. Fig. 2 shows the overall geometry. Like all plasma, the surface properties are both cellular and filamentary, e.g., as shown in Fig. 4, displaying an almost diamond-pattern in the upper cone. The two figures below the plasma photographs are petroglyphs displaying essentially the same morphology as the plasma. Some

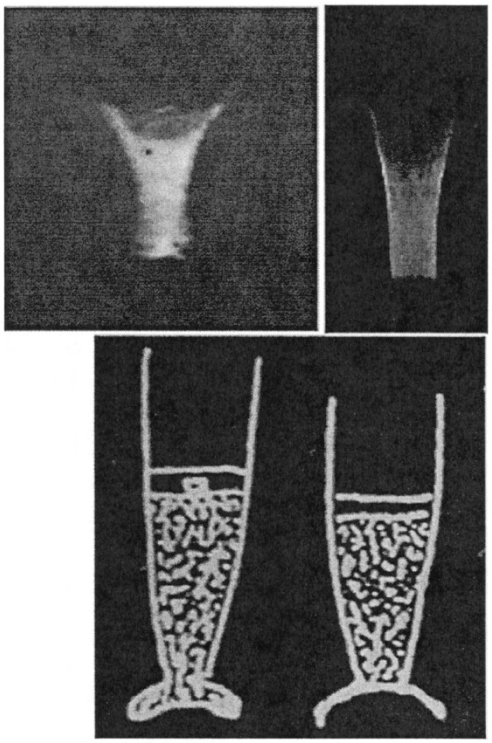

Fig. 38. (Top) Conical inflow of a current conducting plasma column. The flow is from top to bottom. Three important features are already observable: two arm-like shapes at the top of the inflow; striations in the body of the column; and the beginning of a plasma feature at top-center. These experimental photographs pertain to a 5-MV 3-MA plasma. (Bottom) Petroglyphs.

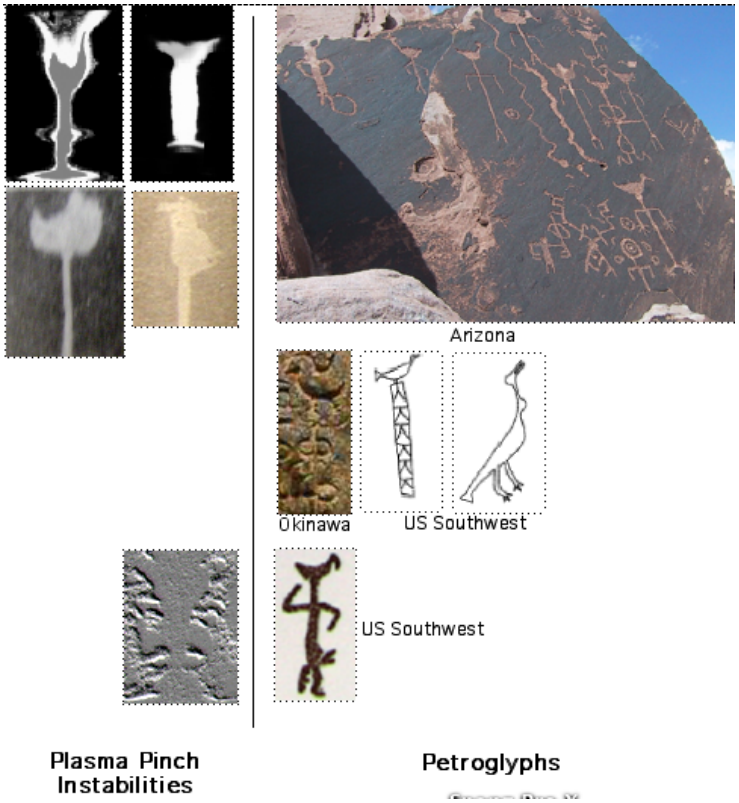

Fig. 39. Experimental data and petroglyphs. (Left) Plasma pinch instabilities. (Right) Petroglyphs relating to birds atop posts and on the heads of man-like figures. The plasma pinch photo at the bottom has been digitally stratified for clarity. The cathode is at the top.

petroglyphs have even captured closely the diamond and filamentary patterns. This will be presented in another paper.

The similarity between petroglyphs and a converging plasma region is shown in Fig. 38. Three important features are observable: two arm-like shapes at the top of the inflow, striations in the body of the column, and plasma feature at top-center. These experimental photographs pertain to a 5-MV, 3-MA plasma.

A. Plasma Cup

Both the cup, a deformed plasma toroid, and the return current are open to a number of interpretations if related to petroglyphs. These show a marked dependency on the cultural background of the petroglyph artist. It can be interpreted as a duck, bird, triangle, or even a head topped by a folded back elephant's trunk. At times, if the return current was sufficiently bright, a snake-head or lightning-bolt head could be interpreted.

Fig. 39 shows some examples of both the plasma top-most geometry and some of the bird-like interpretations.

Fig. 40 is a very common plasma profile. Dependent upon the oblateness and the tilt of the structure, it can be interpreted to represent a duck, a boat, the body of an animal, or an elongated or billed bird (for example Fig. 39); or even a rabbit.

B. Terminus

It is common for plasma clusters to have protrusions very much resembling feet, head, or tails of anthromorphs or animals. The protrusions are part of the termini or filamentary currents running through and from the plasma. An example of termini from an intense discharge is shown below (Fig. 41). In this case,

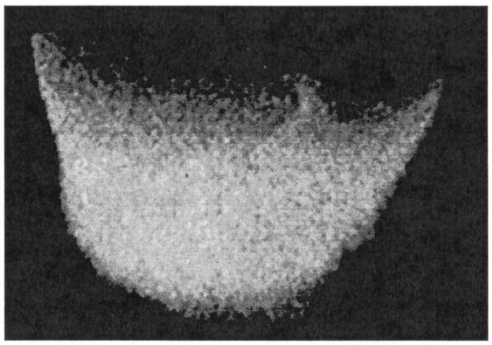

Fig. 40. Experimental plasma photograph of the upper terminus cup of an instability column as shown in Fig. 39, left. This shape can be interpreted to be a duck, a boat, or the body of an animal dependent upon the culture to which the artist belonged. A small perturbation appears two-thirds of the way to the right of this figure. At later times this feature grows into a helical or lightning-like discharge structure.

two discharge strokes have trifurcated at the bottom conductor such as a plasma sheet to allow the current conduction path to continue.

The topology closely resembles petroglyphs of animals: mountain sheep or dogs and foxes in the American Southwest, similar canine species in Australia, and oxen or oxen-like species in other parts of the world. Good examples can be found among the previous digital petroglyph images.

XVI. Shock Phenomena Petroglyphs

A large number of petroglyphs can be connected to the impulse shock instabilities rather than the plasma instabilities.

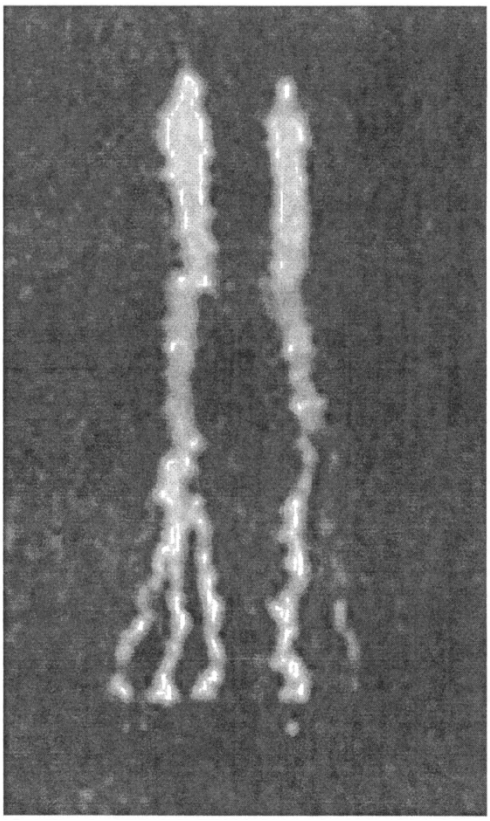

Fig. 41. Example of an electrical discharge that has formed two filamentary currents each of which trifurcate at the bottom to allow the conduction of the current carried in the filaments.

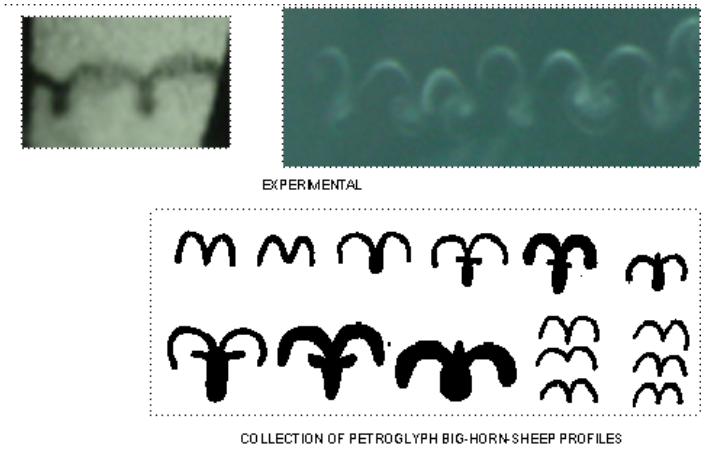

Fig. 42. (Top) Supersonic shocked interface experimental data. (Bottom) Collection of horn profiles from petroglyphs of presumed big-horn-sheep in the Western U.S.

Fig. 42 shows supersonic shocked interface experimental data while at the bottom of the figure are shown a collection of horn profiles from petroglyphs of presumed big horn sheep in the Western U.S.

Another example of a shock initiated hydrodynamic instability is shown in Fig. 43. On the left is an experimental photograph at late time while on the right is a multiple-row mushroom-like petroglyph category depiction.

We now turn to another class of petroglyph, those associated with the upward view on an intense aurora as depicted in Fig. 4.

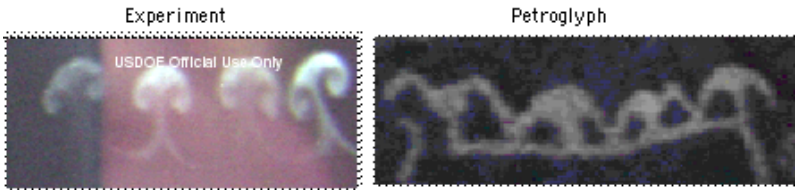

Fig. 43. (Left) Experimental photographs of the mushrooms created in a highly nonlinear plasma column and concomitant shock waves that could occur in auroral plasmas during usual magnetic storms. (Right) Petroglyph.

XVII. Petroglyphs Associated With the Circular Aurora Plasma

Sections II–XVI were concerned with the Z-pinch instabilities that occur along the plasma column as seen in the lower center, right side of Fig. 4. We now turn to images that would be seen in an upward view of the intense aurora (left-side, Fig. 4). These are studied using high-energy-density experiments and objects from antiquity.

A. Megaampere Particle Beams: 56- and 28-Fold Symmetry

A solid beam of charged particles tends to form hollow cylinders that may then filament into individual currents [9]. When observed from below, the pattern consists of circles, circular rings of bright spots, and intense electrical discharge streamers connecting the inner structure to the outer structure.

Fig. 45 shows a 0.6-mm-thick titanium witness plate that has been placed 15 cm in front of a 100 kG, submegaampere charged particle beam. Initially, the particle beam was cylindrical but after traveling the 15 cm has filamented.

The wavelength of filamentation depends on the cylindrical thickness of a hollow beam [9]. In Fig. 45, the beam thickness is 157 μm while the beam radius is 11 mm. In the subgigampere range, the maximum number of self-pinched filaments allowed before the cylindrical magnetic field will no longer split into "islands" for the parameters above has been found to be 56 [53].

Modeling of 56 parallel electrical currents in two and three dimensions was carried out with a large-scale MHD code [54]. These results verify that individual current filaments were maintained by their azimuthal self magnetic fields, a property lost by increasing the number of electrical current filaments.

The scaling is constant for a given hollow beam thickness, from microampere beams to multimegaampere beams and beam diameters of millimeters to thousands of kilometers [9], that is, the same filamentation and vortices apply to auroral plasmas.

Because the electrical current-carrying filaments are parallel, they attract via the Biot-Savart force law, in pairs but sometimes three [8]. This reduces the 56 filaments over time to 28 filaments, hence the 56 and 28 fold symmetry patterns.

In actuality, during the pairing, any number of filaments less than 56 may be recorded as pairing is not synchronized to occur uniformly. However, there are "temporarily stable" (longer state durations) at 42, 35, 28, 14, 7, and 4 filaments. Each pair formation is a vortex that becomes increasing complex, as do the instabilities in today's auroras as they decrease in number by merger.

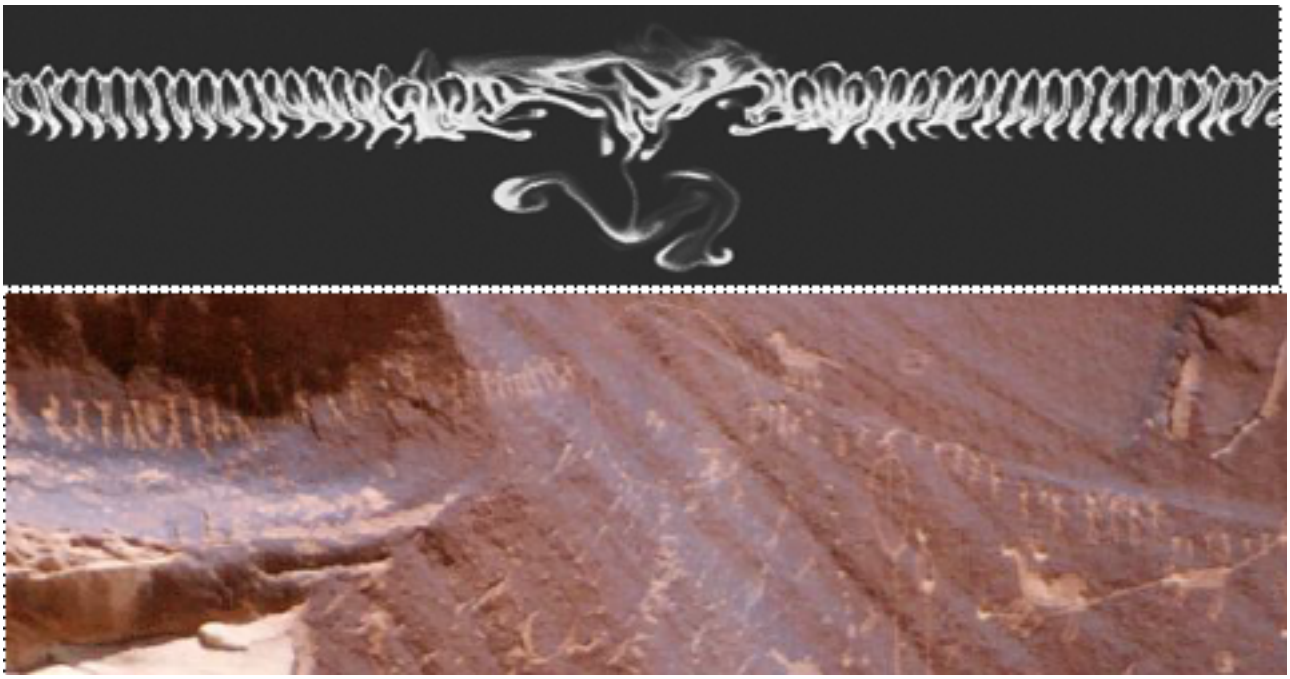

Fig. 44. (Top) Initial instability structure in a thin layer with a density ten times that of the ambient medium surrounding it. A perturbation has been induced in the numerical calculation by shocking the layer at the center with a wave of Mach number 1.2. (Bottom) One sample of this often recorded petroglyph.

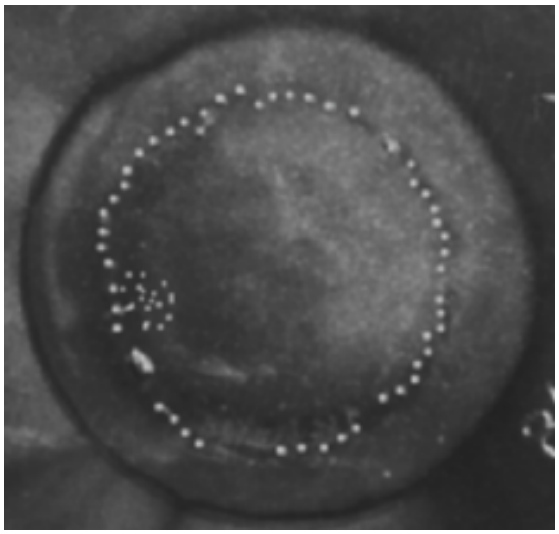

Fig. 45. Steel witness plate with filament hole locations. The hole locations have been digitally enhanced. While the nearly cylindrical beam has a periodicity of 56 holes around the circle, not all of the holes are discernible on the witness plate. Trueness of the ring increases with magnetic field strength. Also recorded on the plate are microcircles of holes within the main ring (e.g, at 8:30, about 1/5 the diameter of the major hole ring) and some beam sheath etching outside the main circle.

B. Records From Antiquity With 56- and 28-Fold Symmetry

The number of 56 and 28 fold symmetry objects from antiquity is manifest. These range from concentrical petroglyphs around the world to geoglyphs (stone-rings), megaliths, and other constructs. The most renowned of the 56 fold symmetric megaliths is Stonehenge.

Stonehenge is a unique structure; a megalithic ruin (51.22° N, 0.167° W) located west of the town of Amesbury, Wiltshire, U.K. [55]–[63].

It is concentric is shape having two outer banks of earth, approximately 100 m in diameter, circular, with gaps. Adjacent the surrounding banks are circular and half-circular ditches, each with a radius of 5–6 m and each having a three-concentric pattern. Within the banks are the Aubrey Holes; now-filled marker holes equally spaced at 56 points around a great circle that cut across the small concentric ditches.

Geometrically inward, the next named feature, are the "Y" holes, 30 in number. These are nearly symmetrically located on a concentrical circle. The next concentrical circle is made up of "Z" holes. Noteworthy of both the "Y" and "Z" holes, in contrast to the other parts of the megalith, is that they are not cylindrically symmetric. Both have a bulge at approximately the same azimuthal position where there is a displacement outwards between neighboring holes. The "Z" hole circle has a large displacement. There are 30 holes on this circle, 28 of which are readily visible.

The next concentric is the Sarsen Circle, 33 m in diameter, originally comprised of 30 upright sandstone blocks standing on average 4 m above the ground. They originally supported Sarsen lintels forming a continuous circle around the top.

Inside the Sarsen circle is the Bluestone Circle. (The term "bluestone" refers to various types of mostly igneous rocks including dolerites, rhyolites, and volcanic ash. It also includes some sandstones. In color they are actually gray-red. The Bluestones at Stonehenge are believed to have originated from various outcrops in the Preseli Hills in southwest Wales. How they were transported to the site at Stonehenge has been the subject of much speculation).

The "bluestones" are on average 1.25 m wide and 0.75 m deep. These pillars stand 1.8 m high and originally numbered 35, periodically placed between the outer sarsen circle and the next concentric, a "horseshoe" of Sarsen Trilithons.

The Trilithons are ten upright stones arranged as five free-standing pairs each with a single horizontal lintel. They were erected within the Sarsen Circle in the form of a horseshoe with the open side facing northeast toward the main entrance of the monument. They were arranged symmetrically and graded in

height; the tallest is in the central position. The Trilithons are the most impressive feature of the monument, the heaviest of which weighs nearly 45 tons.

Inside the Trilithon horseshoe is another horseshoe of bluestone pillars. An "Alter" stone in front of the center Trilithons completes the main structure of Stonehenge.

Additional stones mark the way to the "Avenue" or "Cursus," a 2.8-km-long earthwork in the shape of a "tail" running linearly outwards from the horseshoes for 500 m then curving southeast.

The dating of the construction of Stonehenge by English Heritage [64] from 14 samples, primarily antlers, is 3020–2910 BC for the surrounding ditch and Aubrey holes to 2270–1930 BC for the Bluestone Horseshoe. The Z Holes are estimated at 2850–2480 BC, the same date as given the Sarsen Circle. The concentric nature of the main monument and the inadequacy of the recording of many of the relationships which exist, leads to a shortage of direct stratigraphic relationships [61].

C. "Old" Concentric Petroglyphs and Pictographs With 56- and 28-Fold Symmetry

The "old concentrics" are among the most ancient of petroglyphs and pictographs. The carvings have long since reverted to the coloration of the rock patina onto which they were embedded. The paintings have leached into the rock, greatly dulling their appearance.

As examples of 56-fold symmetric concentrics, we shall take three representative examples. The first is one of the opening plates of "Pictographs and Petroglyphs of The Oregon Country," by Loring and Loring [47]. In particular, plate III, a photograph of their Site 34, 4 O'Clock Rapids on the East Rim, Klickitat County, Washington (45° 42.776 N, 120° 20.970 W, 92 m) (this petroglyph is one that the Lorings described as "outstanding and appeared to be very old." The Lorings, from 1964 to 1968, took many photographs and rubbings of the deeply carved petroglyphs flooded by the J. Day Dam in April 1968).

The second example is a pictograph downstream of 4 O'Clock Rapids at J. Day bar, the Loring's site 29 (45° 44 N, 120° 41 W).

The third example is from northern Arizona (35° N, 109° W), 1450 km SE of the Columbia River Basin.

In Fig. 46 are overlays of these three petroglyphs on a reconstruction image of Stonehenge [65]. Each petroglyph shows slightly different detail. The top left petroglyph has apparently captured a later time image of the aurora as some of the outer dots are starting to undergo a diocotron instability rotational pairing as was also recorded on the witness plate in Fig. 45.

Both of the top overlays have recorded the inter-filament electrical streamers between the inner dot circles (electrical currents in forward synchrotron radiation light emission). The bottom-left petroglyph has recorded the streamers between the two outer dots. (The 4 O'Clock Rapids petroglyph is about 60 cm in diameter while Stonehenge is approximately 100 m in diameter).

However, an anomaly exists as illustrated in Fig. 46, top left. Loring's reproduction shows a ring of outer dots that are not seen in the photograph. Moreover, other photographs of this petroglyph before flooding, show no indication of an outer ring of dots. Mid-twentieth century chalk enhancement photographs also do not provide evidence for the existence of an outer ring of dots.

Through image analysis, we have recovered an outer ring of dots precisely where the Lorings found them. Three of the underside outer holes were protected and still deep. Thus, like Stonehenge, it would appear as if the outer holes were constructed much earlier than the inner holes, time enough for the outer holes to be very nearly worn away (another possibility is that the central features were re-worked over time).

While many such images have been found, we shall cite the next five. The fifth is found 1479 km to the southeast. Two images nearly directly north are found 7466 and 7817 km away, respectively. Another image is 10 715 km to the west and slightly south (no inner structure). The last of the five cited is 8926 km to the northeast.

Fig. 47, top-left, depicts a 56-ray pictograph from the Windjana site at the Wanalirri rock art caves in north-west Kimberley, Western Australia (17.6° S, 126.5° W) [66]. (The thicker rays at the upper-left are part of a partially over-drawn larger pictograph, see the following). The image at the top-right is the Arizona petroglyph shown in Fig. 46.

As drawn, the Windjana has shortened lower streamers and the concentric is elliptical (a "rod" is also drawn to the center of this pictograph). Image analysis allows the two to overlay precisely, to the extent that it is difficult to discern differences in the rays between the two, but only if the Windjana is digitally tilted at an angle of 45.3°. This is shown at the bottom of Fig. 47. The gray-white "embossed" figure is the Arizona petroglyph while the Australian pictograph is the "flat" black overlay. This comparison technique was forced by the nearly exact overlay of the rays of the two, making it difficult to distinguish one from the other.

The apparent number of rays in the Arizona petroglyph is 47, but 56 when the thick ray at 4:00 is separated into three rays, and the thick rays at 9:30, 10:30, and 12:30 are each separated into two.

The need to tilt the Australian pictograph for an exact fit, when projected into space, suggests that the length/size of the intense aurora greatly exceeds that observed today.

Painted over the upper left of the 56-ray Windjana are rays from a second larger Windjana image. This image too has a periodic 56-ray pattern. However, 30% of the rays were never drawn at the bottom of the image. That this is a "younger" image, in addition to it being painted on top of the "older" image is that the tips of the rays apparently have well developed curls or vortices painted as "blobs." The missing bottom most rays also suggest that this is a horizon image.

Other 56-fold images are found as far as 15 000 km away so that different angles of observation should allow the location of the incoming plasma to be determined. For example, Fig. 48 shows "site-34-rings" overlaid on the three petroglyph/pictograph examples and Stonehenge. The site-34-rings were generated from the 4 O'Clock Columbia River petroglyph, then overlaid on the other images. A slight skewness of this petroglyph is apparent toward the lower-right corner as seen in the blind-rings. This indicates a small obliqueness of observation as seen from the Columbia River.

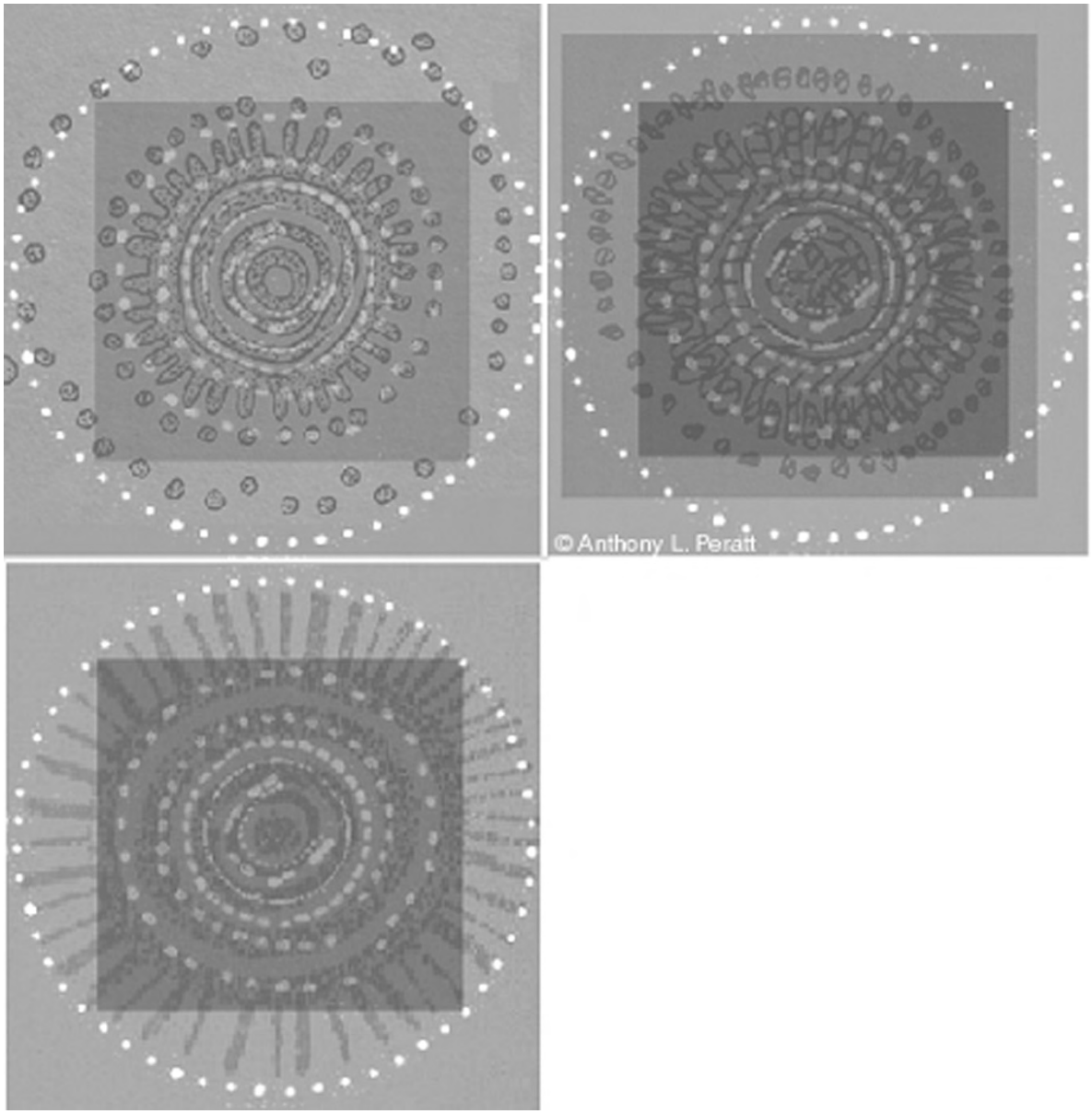

Fig. 46. Overlays of petroglyphs and a pictograph (gray) with a reconstruction image of Stonehenge (white). (Top Left) 4 O'Clock Rapids petroglyph on the Columbia River in the state of Washington. (Top Right) J. D. Bar pictograph, Columbia River. (Bottom Left) Northern Arizona petroglyph. The 4 O'Clock Rapids petroglyph is about 60 cm in diameter while Stonehenge is approximately 100 m in diameter.

Newer concentrics and spirals, easily discerned on rock, generally are less precisely drawn but do include embellishments found in electrical discharges at later time. The evolution of these morphologies will be discussed in another paper.

XVIII. Discussion and Conclusion

A discovery that the basic petroglyph morphologies are the same as those recorded in extremely high-energy-density discharges has opened up a means to unravel the origin of these apparently crude, misdrawn, and jumbled figures found in uncounted numbers around the Earth.

Drawn in heteromac style (Fig. 12), these ancient patterns could mimic and replicate high-energy phenomena that would be recorded on a nonerasable plasma display screen. Many petroglyphs, apparently recorded several millennia ago, have a plasma discharge or instability counterpart, some on a one-to-one or overlay basis. More striking is that the images recorded on rock are the only images found in extreme energy density experiments; no other morphology types or patterns are observed [46], [67].

The instability is that associated with an intense current-carrying column of plasma which undergoes both sausage and helix deformations. Such a current would be produced if the solar flux from the Sun were to increase one or two magnitudes or if another source of plasma were to enter the solar system.

This paper has followed the evolution of a Z-pinch from the initiation of instabilities in a column conducting mild currents (Fig. 16) to the helical and sausage instabilities as the current increases (Figs. 6 and 7) to extremely intense current instabilities (Fig. 36). While the morphing of the instability is a continuous

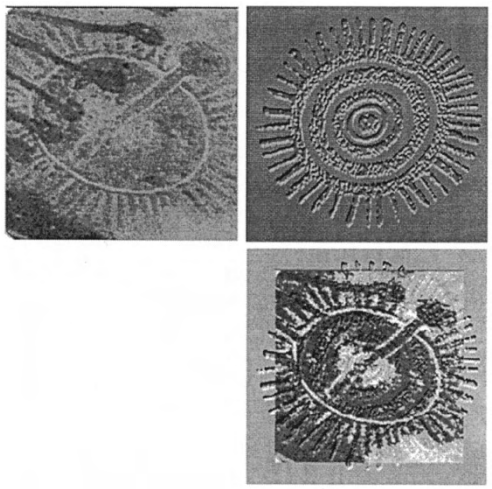

Fig. 47. (Top Left) Windjana pictograph, Australia. (Top Right) Petroglyph, Northern Arizona. (Bottom) Overlay of the Australia and Arizona figures. The gray-white "embossed" figure is the Northern Arizona petroglyph while the Australian pictograph is the "flat" black overlay. The Windjana "ellipse" is fitted to the outer concentric of the Northern Arizona petroglyph.

process to peak current, we have found it convenient to delineate the instability profile into 84 categories (not all are shown in this paper).

The sausage and helical MHD (magnetic-fluid) instabilities occur in the inner cylinder of plasma, pinched by its own azimuthal (surrounding) magnetic fields produced by the intense current it carries. The evolution of this instability is well known in a linear regime that includes the pinching of the column into a stack of spheroid plasmas, usually nine in number, that contain azimuthal current toroids, the original pinch magnetic fields. The electrons with the plasma toroids are relativistic, producing beams of synchrotron radiation observable in the visible. (Hot plasmas emit radiation across the visible and radio spectrum. However, the emission often does not always have a thermal origin).

Collisional processes also produce visible light within the column whose luminosity varies with the current intensity and sporadic current pulses. The luminosity and the observer's position in relation to the column determine how much of the instability is seen.

In familiar terms the linear instability consists of stacks of spheroids, stacks of toroids (Fig. 10), stacks of double radiation bright spots within the toroids, eye-masks, pronounced nose features accompanying the eyes (Fig. 18), and complex X-shaped (separatrix) patterns (the patterns are not shown in this paper).

With increasing current, the instabilities enter the nonlinear and chaotic regime. The effect is a rapid inward motion of the pinch regions so as to form a stack of toroids. These are connected by a central bar running vertically through them. The extreme pressures cause the toroids to flatten and produce a single rod ladder configuration of disks. The next phase of the evolution is the warping and flattening of the disks, which ultimately start to roll-up at the edges producing cup-like, then mushroom instability shapes. The uppermost or anode cups converge and fold to produce a bulb at the very top of the column surrounded by cups in various stages of folding.

Generally, there is a mixture of toroid types throughout the column: tubular, flat, disk, cone, distorted, and cup shapes. Sometimes a single tubular or flat or distorted toroid is left at the center while the bottom-most or cathode consists of a cup that has turned down toward its terminus that may be sheet plasma. The single rod, in all cases, is present at the center of the stack, from top to bottom.

The anode end of the stack is the most interesting, producing various cup shapes and allowing lightning-like discharges to its terminus, although discharges are also observed from the cathode end and sometimes between the toroids or outwards from the toroids for appreciable distances. These are the signatures of high-voltage discharges as are trifurcated bolts found at the ends of any conductor (Fig. 41).

Plasma flowing in along converging magnetic fields produces a well-defined Y shape (Fig. 38). Inflowing plasma, as in an intense aurora (Fig. 4), is marked by a head of circular rings and radial rays (Figs. 4 and 43) and one or two spiral discharge channels along the length of the aurora. Beneath the head, the plasma column shows a number of patterns consisting of horizontal and helical filaments, diamond or separatrix patterns, for example, square vortex patterns as-well-as the previously shown instability shapes.

When a shock wave produced by sporadic current pulses impacts the plasma morphologies mentioned above, these morphologies are altered in striking ways by hydrodynamic instabilities (Fig. 11). Arms become wings and cups become altered by the same instability patterns. These instabilities eventually grow into three-fold pattern such as shown in Fig. 43.

Experimentally, plasmas scale at least 14 orders of magnitude [9] and hypothesized to scale at least 27 orders of magnitude [34] (that is, the instabilities and the growth rates associated with microampere currents are the same, when scaled, to those found in several multimegaampere currents measured *in-situ* in the solar system).

In association with petroglyphs, this indicates that the relative time scales for the MHD instabilities carved in rock follow a known experimental sequence to the extent that time motion sequence of petroglyphs patterns can be generated and put along side the time motion recordings of plasma instabilities. Absolute times cannot, however, be ascertained in this way.

When scaled to an intense aurora whose dimensions may exceed 50 000 km for the outer cusp region, a relative time sequence can be unfolded. For example, the nuances captured in the bottom right images of Fig. 28 can be explained. The inward rise on axis along with the upward folding of the outer edges of the carved lines and transition to edge curling, a phenomena recorded in intense electrical discharge radiographs, could not have been known to prehistoric man unless he witnessed the same event in the sky. Scaling to the plasma dimensions suggests that each of the patterns shown in Fig. 28 could have occurred repeatedly over months or a decade.

The known plasma and shockwave instability types, when scaled from experimental to space plasma dimensions, suggests an intense auroral event lasting at least a few centuries. The newer concentrics, especially those with inner patterns (not shown) and the unwinding spirals provide information about the final cessation of intense incoming plasma flux. On the other

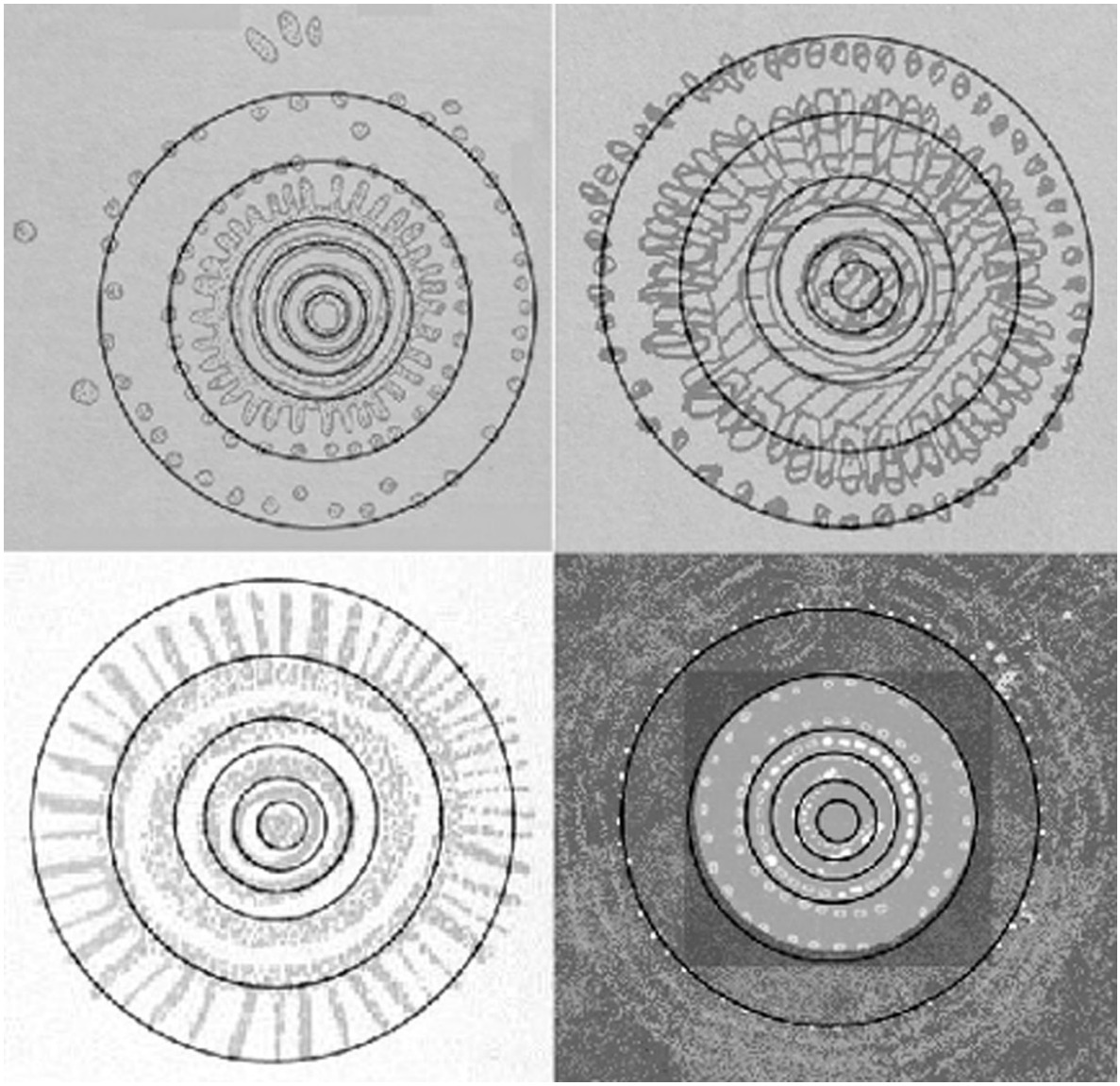

Fig. 48. (Top Left) "Site-34-rings," the mean average radius of a circle as determined by image-object weighting from the 4 O'Clock Rapids petroglyph on the Columbia River. These 4 O'Clock Rapids (Loring Site 34) rings have been overlaid on the other three images. (Top Right) J. Day Bar pictograph. (Bottom Left) Northern Arizona petroglyph. (Bottom Right) Stonehenge reconstruction image (white dots).

hand, the ancient concentrics and spirals, the remains of some having been cut and carved 8 cm deep in granite, suggests that intense auroral events were a common occurrence for at least a few centuries if not millennia. The patterns are representative of a long-term period of typically quiescent aurora.

The methodology used in analyzing petroglyphs and their comparison to extremely high energy density plasmas was based on creating a digital database of several tens of thousands of petroglyphs from around the world. Where possible the following information was included in the database: information about the nature of the physical properties, type of rock used, facing direction, most probable field-of-view, longitude, latitude, altitude, and other petroglyphs in association. Again where possible, the location and facing of the petroglyphs were plotted on 3-D topographic maps in a search for a preferred field-of-view and thus the height and location of the aurora. This analysis is ongoing but initial results suggest three epochs where in a flurry of activity petroglyphs were recorded worldwide. The number of millennia or centuries involved remains unknown.

The discovery of buried horizontal petroglyphs in New Mexico and Australia [51], above which the carbon from campfires was found, suggests that the epochs occurred within a time period of 10 000 BC–2000 BC. This corresponds well with recent plasma extraction dating methods by Rowe and Steelman for pictographs having the same patterns as the petroglyphs in this paper [68].

Two important classes of petroglyphs, spirals and concentric horseshoes, are not discussed in this paper. These map the Birkeland currents as depicted in Fig. 4 and provide quantitative information on the electrical parameters. These, including solar wind-magnetosphere interactions, are being studied with TRISTAN [8], [24], [69] and will be presented elsewhere.

ACKNOWLEDGMENT

The author would like to thank those who contributed data to this paper, in particular: A. Acheson, M. Acheson, K. Anderson, M. Armstrong, H. Arp (MPI, Garching), A. Bodin (LANL), E. J. Bond, D. Cardona, E. Cochrane, F. Costanzo, L. Crumpler (NASA), Z. Dahlen, H. Davis (LANL), A. de Grazia, A. J. Dessler (U. Ariz.), T. E. Eastman (NASA Goddard), J. Goodman, P. Hedlund, G. Heiken (Geo, LANL), H. Johnson, K. Kintner (LANL), J. Lawson (NAVAIR, NAWCWD), B. G. Low, A. S. McEwen, M. Medrano (PNM), F. Minshall (USNPS), M. Minshall, M. Mitchell, K. Moss, J. Nelson (BLM), A. Neuber, S. Parsons, C. M. Pedersen, G. G. Peratt (U. Ariz.), M. G. Peratt (USC), G. Pfeufer (LANL), C. J. Ransom, M. W. Rowe (Texas A&M), T. Scheber (LANL), G. Schwartz (U. Ariz.), A. Scott, D. E. Scott (U. Mass), D. Scudder (LANL), J. Shlacter (LANL), P. Shoaf (NAVAIR, NAWCWD), R. M. Smith (JPL), C. Snell (LANL), D. Talbott, T. Thomsen, W. Thornhill, H. Tresman, I. Tresman, M. A. van der Sluijs, T. Van Flandern (NRL), T. Voss, W. S-Y. Wang (U. Hong Kong), R. Webb, B. Whitley (Ariz. Petro. Steward), P. Whitley (Ariz. Petro. Steward), and E. Younkin (Maturango Museum). He would also like to thank J. McGovern, Georgetown, South Australia; A. B. Mainwaring, S. Mainwaring, and J. A. Sabloff for their continued support, suggestions, and editing of this manuscript; and the Navajo Nation and the Cochiti, San Juan, Santa Clara, Jemez, Santo Domingo and San Ildefonso Pueblos in Northern New Mexico.

REFERENCES

[1] J. A. Van Allen, L. A. Frank, and B. J. O'Brien, "Satellite observations of the artificial radiation belt of July 1962," *J. Geophys. Res.*, vol. 68, no. 3, p. 619, 1963.

[2] J. A. Van Allen, *Origins of Magnetospheric Physics*. Washington, DC: Smithsonian Institution Press, 1983.

[3] A. Egeland and J. Holtet, *The Birkeland Symposium on Aurora and Magnetic Storms*. Paris, France: Centre National de la Recherche Scientifique, 1967.

[4] T. E. Eastman, "Transition regions in solar system and astrophysical plasmas," *IEEE Trans. Plasma Sci.*, vol. 18, pp. 18–25, Feb. 1990.

[5] C.-G. Fälthammar, "Magnetosphere-ionosphere interactions-near earth manifestations of the plasma universe," *IEEE Trans. Plasma Sci.*, vol. PS-14, pp. 616–628, Feb. 1986.

[6] J. R. Kan and S.-I. Akasofu, "Electrodynamics of the solar wind-magnetosphere-ionosphere interactions," *IEEE Trans. Plasma Sci.*, vol. 17, pp. 83–108, Apr. 1989.

[7] C. A. Ekdahl, J. R. Freeman, G. T. Leifeste, R. B. Miller, W. A. Stygar, and B. B. Godfrey, "Axisymmetric hollowing instability of an intense relativistic electron beam propagating in air," *Phys. Rev. Lett.*, vol. 55, no. 9, pp. 935–938, 1985.

[8] A. L. Peratt, *Physics of the Plasma Universe*. New York: Springer-Verlag, 1992.

[9] A. L. Peratt and C. M. Snell, "Microwave generation from filamentation and vortex formation within magnetically confined electron beams," *Phys. Rev. Lett.*, vol. 54, p. 1167, 1985.

[10] A. V. Shishlov, R. B. Baksht, A. Y. Labetsky, V. I. Oreshkin, A. G. Rousskikh, A. V. Fedunin, S. A. Chaikovsky, V. A. Kokshenev, N. E. Kurmaev, and F. I. Fursov, "Experimental study of an argon-hydrogen Z-pinch plasma radiation source," *IEEE Trans. Plasma Sci.*, vol. 30, pp. 486–511, Apr. 2002.

[11] A. Krejci, J. Raus, V. Piffl, A. V. Golubev, Y. Y. Platoov, E. Krousky, and O. Renner, "Multichannel soft X-ray diagnostics of hot plasma evolution in nitrogen-puff Z-pinch," *IEEE Trans. Plasma Sci*, vol. 23, pp. 584–587, Oct. 1993.

[12] C.-G. Fälthammar, "Electrodynamics of cosmical plasmas-some basic aspects of cosmological importance," *IEEE Trans. Plasma Sci.*, vol. 18, pp. 11–17, Feb. 1990.

[13] "Special issue on space plasmas," *IEEE Trans. Plasma Sci.*, vol. 28, Dec. 2000.

[14] H. A. Davis *et al.*, "The atlas high energy density project," *Jpn. J. Appl Phys.*, pt. 1, vol. 40, no. 2B, pp. 930–934, 2001.

[15] R. E. Reinovsky *et al.*, "Stability of magnetically imploded liners for high energy density experiments," in *Proc. 8th Int. Conf. Megagauss Magnetic Field Generation and Related Topics*, Tallahassee, FL, Oct. 1998, p. 309.

[16] A. M. Buyko *et al.*, "Instability growth in magnetically imploded, high strength, cylindrical liners (Results of a joint VNIIEF/LANL experiment on the Pegasus-2 facility)," in *Proc. 8th Int. Conf. Megagauss Magnetic Field Generation and Related Topics*, Tallahassee, FL, Oct. 1998, p. 297.

[17] H. Lee, R. R. Bartsch, R. L. Bowers, W. Anderson, W. L. Atchison, R. E. Chrien, J. Cochrane, H. Oona, D. Platts, M. Rich, W. R. Shanahan, D. W. Scudder, J. Stokes, and L. Veeser, "Megabar liner experiments on pegasus II," in *Proc. 11th IEEE Int. Pulsed Power Conf.*, G. Cooperstein and I. Vitkovitsky, Eds., Baltimore, MD, 1997, p. 366.

[18] W. L. Atchison, R. J. Faehl, and R. E. Reinovsky, "Studies of solid liner instability during magnetic implosion," in *Proc. Nuclear Explosives Code Developers Conf.*, Las Vegas, NV, Oct. 1998, p. 107.

[19] S. Chandrasekhar and E. Fermi, "Problems of gravitational stability in the presence of a magnetic field," *Astrophys. J.*, vol. 118, pp. 116–141, 1953.

[20] V. P. Shafranov, *Reviews of Plasma Physics*, M. A. Leontovich, Ed. New York: Consultants Bureau, 1966, vol. 2.

[21] A. Peratt, J. Green, and D. Nielsen, "Evolution of colliding plasmas," *Phys. Rev. Lett.*, vol. 44, pp. 1767–1770, 1980.

[22] P. Kulhanek, "Particle and field solvers in PM models," *Czech. J. Phys.*, vol. 50, pp. 239–244, 2000.

[23] J. A. Guzik and K. Koch, "Code validation for the ASCI antero project," in *Proc. Nuclear Explosives Code Developers Conf.*, Las Vegas, NV, Oct. 1998.

[24] O. Buneman, T. Neubert, and K.-L. Nishikawa, "Solar wind magnetosphere interaction as simulated by a 3-D, EM particles code," *IEEE Trans. Plasma Sci.*, vol. 20, pp. 810–816, Dec. 1992.

[25] M. G. Haines, S. V. Lebedev, J. P. Chittenden, F. N. Beg, S. N. Bland, and A. E. Dangor, "The past, present, and future of Z-pinches," *Phys. Plasmas*, vol. 7, pp. 1672–1680, 2000.

[26] F. N. Beg, A. E. Dangor, P. Lee, M. Tatarakis, S. L. Niffikeer, and M. G. Haines, "Optical and X-ray observations of carbon and aluminum fiber Z-pinch plasmas," *Plasma Phys. Control. Fusion*, vol. 39, pp. 1–25, 1997.

[27] M. G. Haines, "A three-dimensional model of wire array instability, ablation, and jetting," *IEEE Trans. Plasma Sci.*, vol. 30, pp. 588–592, Apr. 2002.

[28] A. Y. Labetsky, R. B. Baksht, V. I. Oreshkin, A. G. Rousskikh, and A. V. Shishlov, "Experimental study of the effect of Rayleigh-Taylor instabilities on the energy deposition into the plasma of a Z-pinch," *IEEE Trans. Plasma Sci.*, vol. 30, pp. 524–531, Apr. 2002.

[29] A. Ortiz-Tapia and P. Kubes, "Identification of the governing parameters of self-organizing structures in Z-pinch plasmas," *Czech. J. Phys.*, vol. 50, no. Supp.S3, pp. 145–149, 2000.

[30] P. Kubes, K. Kolacek, A. Krejci, J. Kravarik, M. Paduch, and K. Tomaszewski, "Evolution of the gas-puff Z-pinch column," *IEEE Trans. Plasma Sci.*, vol. 26, pp. 1113–1118, Aug. 1998.

[31] D. R. Wells, "Observation of plasma vortex rings," *Phys. Fluids*, vol. 5, pp. 1016–1018, 1962.

[32] D. R. Wells, J. Davidson, L. G. Phadke, J. G. Hirshberg, P. E. Ziajka, and J. Tunstall, "High-temperature, high-density plasma production by vortex-ring compression," *Phys. Rev. Lett.*, vol. 41, pp. 166–170, 1978.

[33] J. Davidson and D. R. Wells, "Interaction between two force-free plasma vortices," *Phys. Fluids*, vol. 22, no. 2, pp. 379–381, 1979.

[34] H. Alfvén, *Cosmic Plasma*. Dordrecht, Germany: Reidel, 1981.

[35] ——, "Double layers and circuits in astrophysics," *IEEE Trans. Plasma Sci.*, vol. PS-14, pp. 763–778, Aug. 1986.

[36] Y. G. Zel'dovich and Y. P. Razier, *Physics of Shock Waves and High-Temperature Hydrodynamic Phenomena*. New York: Dover, 2002.

[37] J. M. Budzinskil and R. F. Benjamin, "An experimental investigation of shock-accelerated heavy gas layer's," Los Alamos, Rep., LAUP-95-012-110, 1995.

[38] P. M. Rightley, P. Vorobieff, R. Martin, and R. F. Benjamin, "Experimental observations of the mixing transition in a shock-accelerated gas curtain," *Phys. Fluids*, vol. 11, pp. 186–200.

[39] J. Kamm, P. Rightley, K. Prestridge, C. Zoldi, R. Benjamin, and P. Vorobieff, "The gas curtain experimental technique and analysis methodologies," Los Alamos Nat. Lab. Univ., LA-UR-01-2573, 2002.

[40] A. B. Kukushkin and V. A. Rantsev-Kartinov, "Self-similarity of plasma networking in a broad range of length scales: From laboratory to cosmic plasmas," *Rev. Sci. Instrum.*, vol. 70, no. 22, pp. 1387–1391, 1999.
[41] A. L. Peratt, "Talking rocks," in *Lecture Series on Celestial Catastrophes in Human Prehistory*. Philadelphia, PA: Center for Ancient Studies, Inst. Environ. Studies, Univ. Pennsylvania Museum Archaeol. Anthropol., 2001.
[42] A. van Humboldt, "Personal narrative of a journey to the equinoctial regions of the new continent," Penquin, London, U.K., 1814-25, 1995.
[43] C. N. Dubelaar, "The petroglyphs in the guinas and adjacent areas of Brazil and Venezuela: An inventory," in *Monumenta Archaeologica*. Los Angeles, CA: Univ. Calif., 1986, vol. 12.
[44] C. Wilks, *Narrative of United States Exploratory Expedition, 1838, 1839, 1840, 1841 and 1842*. Philadelphia, PA: Sherman & Son, 1849, vol. 4.
[45] G. Mallery, *Picture-Writing of the American Indians*. New York: Dover, 1972, vol. 1/2.
[46] F. Petrie, *Decorative Patterns of the Ancient World*. New York: Dover, 1974.
[47] J. M. Loring and L. Loring, "Pictographs and petroglyphs of the oregon country," in *Monograph XXI*. Los Angeles, CA: Inst. Archaeol., Univ. Calif., 1982.
[48] J. H. Thiel, "Rock art in Arizona," State Historic Preservation Office, Proj. 649 286, 1995.
[49] P. Schaafsma, *Indian Rock Art of the Southwest*. Albuquerque, NM: New Mexico School of the American Southwest, Univ. New Mexico Press, 1995.
[50] E. Younkin, *Coso Rock Art-A New Perspective*. Ridgecrest, CA: Maturango Museum, 1998.
[51] J. Flood, *Rock Art of the Dreamtime-Images of Ancient Australia*. Sydney, Australia: Angus and Robertson (Harper Collins), 1997.
[52] K. Tashbayeva, *Petroglyphs of Central Asia*. Samarkand, Uzbekistan: Int. Inst. Central Asian Studies, 2002.
[53] C. M. Snell and A. L. Peratt, "Filaments, vortex structure, and microwaves in magnetically confined electrons beams," *Bull. Amer. Phys. Soc.*, vol. 29, p. 1434, 1984.
[54] M. H. Frese, S. D. Frese, S. E. Rosenthal, M. R. Douglas, and N. F. Roderick, "Computational simulation of initiation and implosion of circular arrays of wires in two and three dimensions," *IEEE Trans. Plasma Sci.*, vol. 30, pp. 593–603, Apr. 2002.
[55] "Science and stonehenge," in *Proc. British Academy 92*, vol. 92, B. Cunliffe and C. Renfrew, Eds., Mar. 1998.
[56] D. Souden, *Stonehenge Revealed*. New York: Facts on File, 1997.
[57] R. Atkinson, *Stonehenge*. London, U.K.: H. Hamilton, 1956.
[58] J.-P. Mohen, *The World of Megaliths*. New York: Facts on File, 1990.
[59] R. Castleden, *The Making of Stonehenge*. London, U.K.: Routledge, 1993.
[60] R. M. J. Cleal, K. E. Walker, and R. Montague, "Stonehenge in its landscape: The twentieth-century excavations," English Heritage Arch, London, U.K., Rep. 10, vol. 10, 1995.
[61] M. J. O'Kelly, *Newgrange*. New York: Thames and Hudson, 1982.
[62] A. Burl, *Prehistoric Avebury*. New Haven, CT: Yale Univ. Press, 1979.
[63] ——, *A Guide to the Stone Circles of Britain, Ireland, and Brittany*. New Haven, CT: Yale Univ. Press, 1995.
[64] English Heritage. "Dating Stonehenge". English Heritage Scientific Dating Service, Northampton, U.K.. [Online]. Available: http://www.eng-h.gov.uk/stoneh/
[65] M. P. Pearson and Ramilisonina, "Stonehenge for the ancestors: The stones pass on the message," *Antiquity*, vol. 72, pp. 308–326, 1998.
[66] I. M. Crawford, *The Art of the Windjana*. Melbourne, Australia: Oxford Univ. Press, 1968, p. 144.
[67] C. Schuster and E. Carpenter, *Patterns That Connect*. New York: Abrams, 1996.
[68] M. W. Rowe and K. L. Steelman, "Radiocarbon dating of rock paintings using plasma-chemical extraction," American Laboratory, 2002.
[69] D. S. Cai, Y. T. Li, C. J. Xiao, and X. Y. Yan, "Three-dimensional electromagnetic particle simulations of the solar wind-magnetosphere interaction with time-varying IMF using HPF TRISTAN code," in *Proc. ISSS-6*. Garching, Germany, 2001, pp. 1–4.
[70] T. Gold, "Large solar outburst in the past," *Pontificiae Academiae Scientiarvm Scripta Varia*, vol. 25, pp. 159–174.

Anthony L. Peratt (S'60–M'63–SM'85–F'99) received the B.S.E.E. degree from California State Polytechnic University, Pomona, in 1964, and the M.S.E.E. degree and the Ph.D. degree in electrical engineering from the University of Southern California (USC), Los Angeles, 1967 and 1971, respectively.

From 1972 to 1979, he was a Staff Member with the Lawrence Livermore National Laboratory, Livermore, CA. From 1975 to 1977, he was a Guest Physicist with the Max Planck Institut für Plasmaphysik, Garching, Germany. From 1981 to the present, he as beeen with the Los Alamos National Laboratory, Los Alamos, NM. In 1985, he was a Guest Scientist with the Alfvén Laboratory, Royal Institute of Technology, Stockholm, Sweden. From 1995 to 1999, he was with the Applied Theoretical Physics Division, Physics Division, Associate Laboratory Directorate for Experimental Programs, and he was a Scientific Advisor to the U.S. Department of Energy. He authored *Physics of the Plasma Universe* (Berlin,Germany: Springer-Verlag, 1992), and was an Editor on *Plasma Astrophysics and Cosmology* (Norwell, MA: Kluwer, 1995) and *Advanced Topics in Space and Astrophysical Plasmas* (Norwell, MA: Kluwer, 1997). He has served as session organizer for space plasmas at the IEEE International Confernce on Plasma Science from 1987–1989. His research interests include numerical and experimental contributions to high-energy density plasmas and intense particle beams, inertial confinement fusion, explosively-driven pulsed power generators, lasers, intense-power-microwave sources, particles, high-energy density phenomena, new concepts in space propulsion and high-performance computing, plasma cosmogony, and cosmology.

Dr. Peratt was the Guest Editor for the IEEE TRANSACTIONS ON PLASMA SCIENCE Special Issues on Space Plasmas in 1986, 1989, 1990, 1992, 2000, and 2003. He was the organizer of the IEEE International Workshops on Space Plasmas in 1989, 1991, 1993, 1995–1998, and 2003. He has been an Associate Editor with the IEEE TRANSACTIONS ON PLASMA SCIENCE sinc 1989. He was an Elected member of the IEEE Nuclear and Plasma Science Society (NPSS) Executive Committee (ExCom) from 1987 to 1989 and from 1995 to 1997. He was the General Chairman of the IEEE International Conference on Plasma Science, Santa Fe, New Mexico, in 1994. He was the IEEE NPSS ExCom Vice Chairman and was elected to the IEEE NPSS Administrative Committee, both in 1997. He received the U.S. Department of Energy Distinguished Performance Award in both 1987 and 1999, the IEEE Distinguished Lecturer Award in 1993, and was a Norwegian Academy of Science and Letters, University of Oslo Physics Department, and Norsk Hydro Kristian Birkeland Lecturer in 1995. He is a member of the American Physical Society, American Astronomical Society, and Eta Kappa Nu.